



Search for Spatial Correlations of Neutrinos with Ultra-high-energy Cosmic Rays

The ANTARES collaboration,

A. Albert^{1,2}, S. Alves³, M. Andre⁴, M. Anghinolfi⁵, M. A.⁶, S. Ardid⁶, J.-J. Aubert⁷, J. Aublin⁸, B. Baret⁸, S. Basa⁹, B. Belhorma¹⁰, M. Bendahman^{8,11}, V. Bertin⁷, S. Biagi¹², M. Bissinger¹³, J. Boumaaza¹¹, M. Bouta¹⁴, M. C. Bouwhuis¹⁵, H. Brâncăș¹⁶, R. Bruijn^{15,17}, J. Brunner⁷, J. Busti⁵, B. Caiffi³, D. Calvo³, A. Capone^{18,19}, L. Caramete¹⁶, J. Carr⁷, V. Carretero³, S. Celli^{18,19}, M. Chabab²⁰, T. N. Chau⁸, R. Cherkaoui El Moursli¹¹, T. Chiarusi²¹, M. Circella²², A. Coleiro⁸, R. Coniglione¹², P. Coyle⁷, A. Creusot⁸, A. F. Diaz²³, C. Distefano¹², I. Di Palma^{18,19}, A. Domi^{15,17}, C. Donzaud^{8,24}, D. Dornic⁷, D. Drouhin^{1,2}, T. Eberl¹³, T. van Eeden¹⁵, D. van Eijk¹⁵, N. El Khayati¹¹, A. Enzenhöfer⁷, P. Fermani^{18,19}, G. Ferrara¹², F. Filippini^{21,25}, L. Fusco⁷, Y. Gatelet⁸, P. Gay^{8,26}, H. Glotin²⁷, R. Gozzini³, R. Gracia Ruiz¹⁵, K. Graf¹³, C. Guidi^{5,28}, S. Hallmann¹³, H. van Haren²⁹, A. J. Heijboer¹⁵, Y. Hello³⁰, J. J. Hernández-Rey³, J. Hössl¹³, J. Hofestädt¹³, F. Huang⁷, G. Illuminati^{8,21,25}, C. W. James³¹, B. Jisse-Jung¹⁵, M. De Jong^{15,32}, P. de Jong^{15,17}, M. Kadler³³, O. Kalekin¹³, U. Katz¹³, N. R. Khan-Chowdhury³, A. Kouchner⁸, I. Kreykenbohm³⁴, V. Kulikovskiy⁵, R. Lahmann¹³, R. Le Breton⁸, S. LeStum⁷, D. Lefèvre³⁵, E. Leonora³⁶, G. Levi^{21,25}, D. Lopez-Coto³⁷, S. Loucatis^{8,38}, L. Maderer⁸, J. Manczak³, M. Marcellin⁹, A. Margiotta^{21,25}, A. Marinelli³⁹, J. A. Martínez-Mora⁶, B. Martino⁷, K. Melis^{15,17}, P. Migliozzi³⁹, A. Moussa¹⁴, R. Muller¹⁵, L. Nauta¹⁵, S. Navas³⁷, E. Nezri⁹, B. Ó. Fearraigh¹⁵, A. Păun¹⁶, G. E. Păvălaş¹⁶, C. Pellegrino^{21,40,41}, M. Perrin-Terrin⁷, V. Pestel¹⁵, P. Piattelli¹², C. Pieterse³, C. Poiré⁶, V. Popa¹⁶, T. Pradier¹, N. Randazzo³⁶, D. Real³, S. Reck¹³, G. Riccobene¹², A. Romanov^{5,28}, A. Sánchez-Losa^{3,22}, F. Salesa Greus³, D. F. E. Samtleben^{15,32}, M. Sanguineti^{5,28}, P. Sapienza¹², J. Schnabel¹³, J. Schumann¹³, F. Schüssler³⁸, J. Seneca¹⁵, M. Spurio^{21,25}, Th. Stolarczyk³⁸, M. Taiuti¹¹, Y. Tayalati¹¹, S. J. Tingay³¹, B. Vallage^{8,38}, V. Van Elewyck^{8,42}, F. Versari^{8,21,25}, S. Viola¹², D. Vivolo^{39,43}, J. Wilms³⁴, S. Zavatarelli⁵, A. Zegarelli^{18,19}, J. D. Zornoza³, J. Zúñiga³

The IceCube collaboration,

R. Abbasi⁴⁴, M. Ackermann⁴⁵, J. Adams⁴⁶, J. A. Aguilar⁴⁷, M. Ahlers⁴⁸, M. Ahrens⁴⁹, J. M. Alameddine⁵⁰, C. Alispach⁵¹, A. A. Alves Jr.⁵², N. M. Amin⁵³, K. Andeen⁵⁴, T. Anderson⁵⁵, G. Anton⁵⁶, C. Argüelles⁵⁷, Y. Ashida⁵⁸, S. Axani⁵⁹, X. Bai⁶⁰, A. Balagopal V.⁵⁸, A. Barbano⁵¹, S. W. Barwick⁶¹, B. Bastian⁴⁵, V. Basu⁵⁸, S. Baur⁴⁷, R. Bay⁶², J. J. Beatty^{63,64}, K.-H. Becker⁶⁵, J. Becker Tjus⁶⁶, C. Bellenghi⁶⁷, S. BenZvi⁶⁸, D. Berley⁶⁹, E. Bernardini^{45,70}, D. Z. Besson⁷¹, G. Binder^{62,72}, D. Bindig⁶⁵, E. Blaufuss⁶⁹, S. Blot⁴⁵, M. Boddenberg⁷³, F. Bontempo⁵², J. Borowka⁷³, S. Böser⁷⁴, O. Botner⁷⁵, J. Böttcher⁷³, E. Bourbeau⁴⁸, F. Bradascio⁴⁵, J. Braun⁵⁸, B. Brinson⁷⁶, S. Bron⁵¹, J. Brostean-Kaiser⁴⁵, S. Browne⁷⁷, A. Burgman⁷⁵, R. T. Burley⁷⁸, R. S. Busse⁷⁹, M. A. Campana⁸⁰, E. G. Carnie-Bronca⁷⁸, C. Chen⁷⁶, Z. Chen⁸¹, D. Chirkin⁵⁸, K. Choi⁸², B. A. Clark⁸³, K. Clark⁸⁴, L. Classen⁷⁹, G. H. Collin⁵⁹, J. M. Conrad⁵⁹, P. Coppin⁸⁵, P. Correa⁸⁵, D. F. Cowen^{55,86}, R. Cross⁶⁸, C. Dappen⁷³, P. Dave⁷⁶, C. De Clercq⁸⁵, J. J. DeLaunay⁸⁷, D. Delgado López⁵⁷, H. Dembinski⁵³, K. Deoskar⁴⁹, A. Desai⁵⁸, P. Desiati⁵⁸, K. D. de Vries⁸⁵, G. de Wasseige⁸⁸, M. de With⁸⁹, T. DeYoung⁸³, A. Diaz⁵⁹, J. C. Díaz-Vélez⁵⁸, M. Dittmer⁷⁹, H. Dujmovic⁵², M. Dunkman⁵⁵, M. A. DuVernois⁵⁸, E. Dvorak⁶⁰, T. Ehrhardt⁷⁴, P. Eller⁶⁷, H. Erpenbeck⁷³, J. Evans⁶⁹, P. A. Evenson⁵³, K. L. Fan⁶⁹, A. R. Fazely⁹⁰, A. Fedynitch⁹¹, N. Feigl⁸⁹, S. Fiedlschuster⁵⁶, A. T. Fienberg⁵⁵, K. Filimonov⁶², C. Finley⁴⁹, L. Fischer⁴⁵, D. Fox⁸⁶, A. Franckowiak^{45,66}, E. Friedman⁶⁹, A. Fritz⁷⁴, P. Fürst⁷³, T. K. Gaisser⁵³, J. Gallagher⁹², E. Ganster⁷³, A. Garcia⁵⁷, S. Garrappa⁴⁵, L. Gerhardt⁷², A. Ghadimi⁸⁷, C. Glaser⁷⁵, T. Glauch⁶⁷, T. Glüsenkamp⁵⁶, J. G. Gonzalez⁵³, S. Goswami⁸⁷, D. Grant⁸³, T. Grégoire⁵⁵, S. Griswold⁶⁸, C. Günther⁷³, P. Gutjahr⁵⁰, C. Haack⁶⁷, A. Hallgren⁷⁵, R. Halliday⁸³, L. Halve⁷³, F. Halzen⁵⁸, M. Ha Minh⁶⁷, K. Hanson⁵⁸, J. Hardin⁵⁸, A. A. Harnisch⁸³, A. Haungs⁵², D. Hebecker⁸⁹, K. Helbing⁶⁵, F. Henningsen⁶⁷, E. C. Hettinger⁸³, S. Hickford⁶⁵, J. Hignight⁹³, C. Hill⁹⁴, G. C. Hill⁷⁸, K. D. Hoffman⁶⁹, R. Hoffmann⁶⁵, B. Hokanson-Fasig⁵⁸, K. Hoshina^{58,95}, M. Huber⁶⁷, T. Huber⁵², K. Hultqvist⁴⁹, M. Hünnefeld⁵⁰, R. Hussain⁵⁸, K. Hymon⁵⁰, S. In⁸², N. Iovine⁴⁷, A. Ishihara⁹⁴, M. Jansson⁴⁹, G. S. Japaridze⁹⁶, M. Jeong⁸², M. Jin⁵⁷, B. J. P. Jones⁹⁷, D. Kang⁵², W. Kang⁸², X. Kang⁸⁰, A. Kappes⁷⁹, D. Kappesser⁷⁴, L. Kardum⁵⁰, T. Karg⁴⁵, M. Karl⁶⁷, A. Karle⁵⁸, M. Kauer⁵⁸, M. Kellermann⁷³, J. L. Kelley⁵⁸, A. Kheirandish⁵⁵, K. Kin⁹⁴, T. Kintscher⁴⁵, J. Kiryluk⁸¹, S. R. Klein^{62,72}, R. Koirlala⁵³, H. Kolanoski⁸⁹, T. Kontrimas⁶⁷, L. Köpke⁷⁴, C. Kopper⁸³, S. Kopper⁸⁷, D. J. Koskinen⁴⁸, P. Koundal⁵², M. Kovacevich⁸⁰, M. Kowalski^{45,89}, T. Kozyneks⁴⁸, E. Kun⁶⁶, N. Kurashashi⁸⁰, N. Lad⁴⁵, C. Lagunas Gualda⁴⁵, J. L. Lanfranchi⁵⁵, M. J. Larson⁶⁹, F. Lauber⁶⁵, J. P. Lazar^{57,58}, J. W. Lee⁸², K. Leonard⁵⁸, A. Leszczyńska⁷⁷, Y. Li⁵⁵, M. Lincetto⁶⁶, Q. R. Liu⁵⁸, M. Liubarska⁹³, E. Lohfink⁷⁴, C. J. Lozano Mariscal⁷⁹, F. Lucarelli⁵¹, A. Ludwig^{83,98}, W. Luszczak⁵⁸, Y. Lyu^{62,72}, W. Y. Ma⁴⁵, J. Madsen⁵⁸, K. B. M. Mahn⁸³, Y. Makino⁵⁸, S. Mancina⁵⁸, I. Martinez-Soler⁵⁷, R. Maruyama⁹⁹, K. Mase⁹⁴, T. McElroy⁹³, F. McNally¹⁰⁰, J. V. Mead⁴⁸, K. Meagher⁵⁸, S. Mechbal⁴⁵, A. Medina⁶⁴, M. Meier⁹⁴, S. Meighen-Berger⁶⁷, J. Micallef⁸³, D. Mockler⁴⁷, T. Montaruli⁵¹, R. W. Moore⁹³, R. Morse⁵⁸, M. Mouhai⁵⁹, R. Naab⁴⁵, R. Nagai⁹⁴, U. Naumann⁶⁵, J. Necker⁴⁵, L. V. Nguyen⁸³, H. Niederhausen⁸³, M. U. Nisa⁸³, S. C. Nowicki⁸³, A. Obertacke Pollmann⁶⁵, M. Oehler⁵², B. Oeyen¹⁰¹, A. Olivas⁶⁹, E. O'Sullivan⁷⁵, H. Pandya⁵³, D. V. Pankova⁵⁵, N. Park⁸⁴, G. K. Parker⁹⁷, E. N. Paudel⁵³, L. Paul⁵⁴, C. Pérez de los Heros⁵, L. Peters⁷³, J. Peterson⁵⁸, S. Philippen⁷³, S. Pieper⁶⁵, M. Pittermann⁷⁷, A. Pizzuto⁵⁸, M. Plum⁵⁴, Y. Popovych⁷⁴, A. Porcelli¹⁰¹, M. Prado Rodriguez⁵⁸, P. B. Price⁶², B. Pries⁸³, G. T. Przybylski⁷², C. Raab⁴⁷, J. Rack-Helleis⁷⁴, A. Raissi⁴⁶, M. Rameez⁴⁸, K. Rawlins¹⁰², I. C. Rea⁶⁷, A. Rehman⁵³, P. Reichherzer⁶⁶, R. Reimann⁷³, G. Renzi⁴⁷, E. Resconi⁶⁷, S. Reusch⁴⁵, W. Rhode⁵⁰, M. Richman⁸⁰, B. Riedel⁵⁸, E. J. Roberts⁷⁸,

S. Robertson^{62,72}, G. Roellinghoff⁸², M. Rongen⁷⁴, C. Rott^{82,103}, T. Ruhe⁵⁰, D. Ryckbosch¹⁰¹, D. Rysewyk Cantu⁸³, I. Safa^{57,58}, J. Saffer⁷⁷, S. E. Sanchez Herrera⁸³, A. Sandrock⁵⁰, M. Santander⁸⁷, S. Sarkar¹⁰⁴, S. Sarkar⁹³, K. Satalecka⁴⁵, M. Schaufel⁷³, S. Schindler⁵⁶, T. Schmidt⁶⁹, A. Schneider⁵⁸, J. Schneider⁵⁶, F. G. Schröder^{52,53}, L. Schumacher⁶⁷, G. Schwefer⁷³, S. Sclafani⁸⁰, D. Seckel⁵³, S. Seunarine¹⁰⁵, A. Sharma⁷⁵, S. Shefali⁷⁷, M. Silva⁵⁸, B. Skrzypek⁵⁷, B. Smithers⁹⁷, R. Snihur⁵⁸, J. Soedingrekso⁵⁰, D. Soldin⁵³, C. Spannfellner⁶⁷, G. M. Spiczak¹⁰⁵, C. Spiering⁴⁵, J. Stachurska⁴⁵, M. Stamatikos⁶⁴, T. Stanev⁵³, R. Stein⁴⁵, J. Stettner⁷³, A. Steuer⁷⁴, T. Stezelberger⁷², T. Stürwald⁶⁵, T. Stuttard⁴⁸, G. W. Sullivan⁶⁹, I. Taboada⁷⁶, S. Ter-Antonyan⁹⁰, S. Tilav⁵³, F. Tischbein⁷³, K. Tollefson⁸³, C. Tönnis¹⁰⁶, S. Toscano⁴⁷, D. Tosi⁵⁸, A. Trettin⁴⁵, M. Tselengidou⁵⁶, C. F. Tung⁷⁶, A. Turcati⁶⁷, R. Turcotte⁵², C. F. Turley⁵⁵, J. P. Twagirayezu⁸³, B. Ty⁵⁸, M. A. Unland Elorrieta⁷⁹, N. Valtonen-Mattila⁷⁵, J. Vandenbroucke⁵⁸, N. van Eijndhoven⁸⁵, D. Vannerom⁵⁹, J. van Santen⁴⁵, S. Verpoest¹⁰¹, C. Walck⁴⁹, T. B. Watson⁹⁷, C. Weaver⁸³, P. Weigel⁵⁹, A. Weindl⁵², M. J. Weiss⁵⁵, J. Weldert⁷⁴, C. Wendt⁵⁸, J. Werthebach⁵⁰, M. Weyrauch⁷⁷, N. Whitehorn^{83,98}, C. H. Wiebusch⁷³, D. R. Williams⁸⁷, M. Wolf⁶⁷, K. Woschnagg⁶², G. Wrede⁵⁶, J. Wulff⁶⁶, X. W. Xu⁹⁰, J. P. Yanez⁹³, S. Yoshida⁹⁴, S. Yu⁸³, T. Yuan⁵⁸, Z. Zhang⁸¹, P. Zhelnin⁵⁷

The Pierre Auger Collaboration,

P. Abreu¹⁰⁷, M. Aglietta^{108,109}, J. M. Albury¹¹⁰, I. Allekotte¹¹¹, K. Almeida Cheminant¹¹², A. Almela^{113,114}, J. Alvarez-Muñiz¹¹⁵, R. Alves Batista¹¹⁶, G. A. Anastasi^{108,109}, L. Anchordoqui¹¹⁷, B. Andrade¹¹³, S. Andringa¹⁰⁷, C. Aramo¹¹⁸, P. R. Araújo Ferreira¹¹⁹, E. Arnone^{109,120}, J. C. Arteaga Velázquez¹²¹, H. Asorey¹¹³, P. Assis¹⁰⁷, G. Avila¹²², A. M. Badesu¹²³, A. Bakalova¹²⁴, A. Balaceanu¹²⁵, F. Barbato^{126,127}, J. A. Bellido^{110,128}, C. Berat¹²⁹, M. E. Bertaina^{109,120}, X. Bertou¹¹¹, G. Bhatta¹¹², P. L. Biermann¹³⁰, V. Binet¹³¹, K. Bismarck^{113,132}, T. Bister¹¹⁹, J. Biteau¹³³, J. Blazek¹²⁴, C. Bleve¹²⁹, J. Blümmer¹³⁴, M. Boháčová¹²⁴, D. Boncioli^{127,135}, C. Bonifazi^{136,137}, L. Bonneau Arbeletche¹³⁸, N. Borodai¹¹², A. M. Botti¹¹³, J. Brack¹³⁹, T. Bretz¹¹⁹, P. G. Brichetto Orchera¹¹³, F. L. Brieche¹¹⁹, P. Buchholz¹⁴⁰, A. Bueno¹⁴¹, S. Buitink¹⁴², M. Buscemi¹⁴³, M. Büsken^{113,132}, K. S. Caballero-Mora¹⁴⁴, L. Caccianiga^{145,146}, F. Canfora^{116,147}, I. Caracas¹⁴⁸, R. Caruso^{143,149}, A. Castellina^{108,109}, F. Catalani¹⁵⁰, G. Cataldi¹⁵¹, L. Cazon¹¹⁵, M. Cerda¹⁵², J. A. Chinellato¹³⁸, J. Chudoba¹²⁴, L. Chytka¹⁵³, R. W. Clay¹¹⁰, A. C. Cobos Cerutti¹⁵⁴, R. Colalillo^{118,155}, A. Coleman¹⁵⁶, M. R. Coluccia¹⁵¹, R. Conceição¹⁰⁷, A. Condorelli^{126,127}, G. Consolati^{146,157}, F. Contreras¹²², F. Convenga¹³⁴, D. Correia dos Santos¹⁵⁸, C. E. Covault¹⁵⁹, S. Dasso^{160,161}, K. Daumiller¹³⁴, B. R. Dawson¹¹⁰, J. A. Day¹¹⁰, R. M. de Almeida¹⁵⁸, J. de Jesús^{113,134}, S. J. de Jong^{116,147}, J. R. T. de Mello Neto^{137,162}, I. De Miti^{126,127}, J. de Oliveira¹⁶³, D. de Oliveira Franco¹³⁸, F. de Palma^{151,164}, V. de Souza¹⁶⁵, E. De Vito^{151,164}, A. Del Popolo^{143,149}, M. del Río¹²², O. Deligny¹⁶⁶, L. Deval^{113,134}, A. di Matteo¹⁰⁹, M. Dobre¹²⁵, C. Dobrigkeit¹³⁸, J. C. D'Olivo¹⁶⁷, L. M. Domingues Mendes¹⁰⁷, R. C. dos Anjos¹⁶⁸, M. T. Dova¹⁶⁹, J. Ebr¹²⁴, R. Engel^{132,134}, I. Epicoco^{151,164}, M. Erdmann¹¹⁹, C. O. Escobar¹⁷⁰, A. Etchegoyen^{113,114}, H. Falcke^{116,147,171}, J. Farmer¹⁷², G. Farrar¹⁷³, A. C. Fauth¹³⁸, N. Fazzini¹⁷⁰, F. Feldbusch¹⁷⁴, F. Fenn^{109,120}, B. Fick¹⁷⁵, J. M. Figueira¹¹³, A. Filipčič^{176,177}, T. Fitoussi¹³⁴, T. Fodran¹¹⁶, T. Fujii^{172,178}, A. Fuster^{113,114}, C. Galea¹¹⁶, C. Galelli^{145,146}, B. García¹⁵⁴, A. L. Garcia Vegas¹¹⁹, H. Gemmeke¹⁷⁴, F. Gesualdi^{113,134}, A. Gherghel-Lascu¹²⁵, P. L. Ghia¹⁶⁶, U. Giaccari¹¹⁶, M. Giannì¹⁴⁶, J. Glombitza¹¹⁹, F. Gobbi¹⁵², F. Gollan¹¹³, G. Golup¹¹¹, M. Gómez Berisso¹¹¹, P. F. Gómez Vitale¹²², J. P. Gongora¹²², J. M. González¹¹¹, N. González¹⁷⁹, I. Goos^{111,134}, D. Góra¹¹², A. Gorgi^{108,109}, M. Gottowik¹⁴⁸, T. D. Grubb¹¹⁰, F. Guarino^{118,155}, G. P. Guedes¹⁸⁰, E. Guido^{109,120}, S. Hahn^{113,134}, P. Hamal¹²⁴, M. R. Hampel¹¹³, P. Hansen¹⁶⁹, D. Harari¹¹¹, V. M. Harvey¹¹⁰, T. Hebbeker¹¹⁹, D. Heck¹³⁴, C. Hojvat¹⁷⁰, J. R. Hörandel^{116,147}, P. Horvath¹⁵³, M. Hrabovsky¹⁵³, T. Huege^{134,142}, A. Insolia^{143,149}, P. G. Isar¹⁸¹, P. Janecek¹²⁴, J. A. Johnsen¹⁸², J. Jurysek¹²⁴, A. Kääpä¹⁴⁸, K. H. Kampert¹⁴⁸, N. Karastathis¹³⁴, B. Keilhauer¹³⁴, A. Khakurdikar¹¹⁶, V. V. Kizakke Covilakam^{113,134}, H. O. Klages¹³⁴, M. Kleifges¹⁷⁴, J. Kleinfellner¹⁵², F. Knapp¹³², N. Kunka¹⁷⁴, B. L. Lago¹⁸³, R. G. Lang¹¹⁵, N. Langner¹¹⁹, M. A. Leigui de Oliveira¹⁸⁴, V. Lenok¹³⁴, A. Letessier-Selvon¹⁸⁵, I. Lhenry-Yvon¹⁶⁶, D. Lo Presti^{143,149}, L. Lopes¹⁰⁷, R. López¹⁸⁶, L. Lu¹⁸⁷, Q. Luce¹³², J. P. Lundquist¹⁷⁷, A. Machado Payeras¹³⁸, G. Mancarella^{151,164}, D. Mandat¹²⁴, B. C. Manning¹¹⁰, J. Manshanden¹⁸⁸, P. Mantsch¹⁷⁰, S. Marafico¹⁶⁶, F. M. Mariani^{145,146}, A. G. Mariazzi¹⁶⁹, I. C. Mariş¹⁷⁹, G. Marsella^{143,189}, D. Martello^{151,164}, S. Martinelli^{113,134}, O. Martínez Bravo¹⁸⁶, M. Mastrodicasa^{127,135}, H. J. Mathes¹³⁴, J. Matthews¹⁹⁰, G. Matthiae^{191,192}, E. Mayotte^{148,182}, S. Mayotte¹⁸², P. O. Mazur¹⁷⁰, G. Medina-Tanco¹⁶⁷, D. Melo¹¹³, A. Menshikov¹⁷⁴, S. Michal¹⁵³, M. I. Micheletti¹³¹, L. Miramonti^{145,146}, S. Mollerach¹¹¹, F. Montanet¹²⁹, L. Morejon¹⁴⁸, C. Morello^{108,109}, M. Mostafá¹⁹³, A. L. Müller¹²⁴, M. A. Muller¹³⁸, K. Mulrey^{116,147}, R. Mussa¹⁰⁹, M. Muzio¹⁷³, W. M. Namasaka¹⁴⁸, A. Nasr-Esfahani¹⁴⁸, L. Nellen¹⁶⁷, G. Nicora¹⁹⁴, M. Niculescu-Oglizanu¹²⁵, M. Niechciol¹⁴⁰, D. Nitz¹⁷⁵, D. Nosek¹⁹⁵, V. Novotny¹⁹⁵, L. Nožka¹⁵³, A. Nucita^{151,164}, L. A. Núñez¹⁹⁶, C. Oliveira¹⁶⁵, M. Palatka¹²⁴, J. Pallotta¹⁹⁴, P. Papenbreer¹⁴⁸, G. Parente¹¹⁵, A. Parra¹⁸⁶, J. Pawlowsky¹⁴⁸, M. Pech¹²⁴, J. Pékala¹¹², R. Pelayo¹⁹⁷, J. Peña-Rodriguez¹⁹⁶, E. E. Pereira Martins^{113,132}, J. Perez Armand¹⁹⁸, C. Pérez Bertolli^{113,134}, M. Perlin^{113,134}, L. Perrone^{151,164}, S. Petrera^{126,127}, C. Petrucci^{127,135}, T. Pierog¹³⁴, M. Pimenta¹⁰⁷, V. Pirronello^{143,149}, M. Platino¹¹³, B. Pont¹¹⁶, M. Pothast^{116,147}, P. Privitera¹⁷², M. Prouza¹²⁴, A. Puyleart¹⁷⁵, S. Querchfeld¹⁴⁸, J. Rautenberg¹⁴⁸, D. Ravignani¹¹³, M. Reininghaus^{113,134}, J. Ridky¹²⁴, F. Riehn¹⁰⁷, M. Risso¹⁴⁰, V. Rizi^{127,135}, W. Rodrigues de Carvalho¹¹⁶, J. Rodriguez Rojo¹²², M. J. Roncoroni¹¹³, S. Rossoni¹⁸⁸, M. Roth¹³⁴, E. Roulet¹¹¹, A. C. Rovero¹⁶⁰, P. Ruehl¹⁴⁰, A. Saftoiu¹²⁵, M. Saharan¹¹⁶, F. Salamida^{127,135}, H. Salazar¹⁸⁶, G. Salina¹⁹², J. D. Sanabria Gomez¹⁹⁶, F. Sánchez¹¹³, E. M. Santos¹⁹⁸, E. Santos¹²⁴, F. Sarazin¹⁸², R. Sarmento¹⁰⁷, C. Sarmiento-Cano¹⁴³, R. Sato¹²², P. Savina¹⁸⁷, C. M. Schäfer¹³⁴, V. Scherini^{151,164}, H. Schieler¹³⁴, M. Schimassee^{113,132}, M. Schimp¹⁴⁸, F. Schlüter^{113,134}, D. Schmidt¹³², O. Scholten¹⁴², H. Schoorlemmer^{116,147}, P. Schovánek¹²⁴, J. Schulte¹¹⁹, T. Schulz¹³⁴, S. J. Sciutto¹⁶⁹, M. Scornavacche^{113,134}, A. Segreto^{143,199}, S. Sehgal¹⁴⁸, R. C. Shellard²⁰⁰, G. Sigl¹⁸⁸, G. Silli^{113,134}, O. Sima^{125,201},

R. Smau¹²⁵, R. Šmíd¹⁷², P. Sommers¹⁹³, J. F. Soriano¹¹⁷, R. Squartini¹⁵², M. Stadelmaier^{113,134}, D. Stanca¹²⁵, S. Stanič¹⁷⁷, J. Stasielak¹¹², P. Stassi¹²⁹, A. Streich^{113,132}, M. Suárez-Durán¹⁷⁹, T. Sudholz¹¹⁰, T. Suomijärvi¹³³, A. D. Supanitsky¹¹³, Z. Szadkowski²⁰², A. Tapia²⁰³, C. Taricco^{109,120}, C. Timmermans^{116,147}, O. Tkachenko¹³⁴, P. Tobiska¹²⁴, C. J. Todero Peixoto¹⁵⁰, B. Tomé¹⁰⁷, Z. Torrés¹²⁹, A. Travaini¹⁵², P. Travnicek¹²⁴, C. Trimarelli^{127,135}, M. Tueros¹⁶⁹, R. Ulrich¹³⁴, M. Unger¹³⁴, L. Vaclavek¹⁵³, M. Vacula¹⁵³, J. F. Valdés Galicia¹⁶⁷, L. Valore^{118,155}, E. Varela¹⁸⁶, A. Vásquez-Ramírez¹⁹⁶, D. Veberič¹³⁴, C. Ventura¹⁶², I. D. Vergara Quispe¹⁶⁹, V. Verzi¹⁹², J. Vicha¹²⁴, J. Vink²⁰⁴, S. Vorobiov¹⁷⁷, H. Wahlberg¹⁶⁹, C. Watanabe¹³⁷, A. A. Watson²⁰⁵, L. Wiencke¹⁸², H. Wilczyński¹¹², D. Wittkowski¹⁴⁸, B. Wundheiler¹¹³, A. Yushkov¹²⁴, O. Zapparrata¹⁷⁹, E. Zas¹¹⁵, D. Zavrtanik^{176,177}, M. Zavrtanik^{176,177}, L. Zehrer¹⁷⁷

The Telescope Array collaboration,

T. Abu-Zayyad^{206,207}, M. Allen²⁰⁷, Y. Arai²⁰⁸, R. Arimura²⁰⁸, E. Barcikowski²⁰⁷, J. W. Belz²⁰⁷, D. R. Bergman²⁰⁷, S. A. Blake²⁰⁷, I. Buckland²⁰⁷, R. Cady²⁰⁷, B. G. Cheon²⁰⁹, J. Chiba²¹⁰, M. Chikawa²¹¹, K. Fujisue²¹¹, K. Fujita²⁰⁸, R. Fujiwara²⁰⁸, M. Fukushima²¹¹, R. Fukushima²⁰⁸, G. Furlich²⁰⁷, N. Globus^{212,213,214}, R. Gonzalez²⁰⁷, W. Hanlon²⁰⁷, M. Hayashi²¹⁵, N. Hayashida²¹⁶, H. He²¹⁴, K. Hibino²¹⁶, R. Higuchi²¹¹, K. Honda²¹⁷, D. Ikeda²¹⁶, T. Inadomi²¹⁵, N. Inoue²¹⁸, T. Ishii²¹⁷, H. Ito²¹⁴, D. Ivanov²⁰⁷, H. Iwakura²¹⁵, A. Iwasaki²⁰⁸, H. M. Jeong²¹⁹, S. Jeong²¹⁹, C. C. H. Jui²⁰⁷, K. Kadota²²⁰, F. Kakimoto²¹⁶, O. Kalashev²²¹, K. Kasahara²²², S. Kasami²²³, S. Kawakami²⁰⁸, S. Kawana²¹⁸, K. Kawata²¹¹, I. Kharuk²²¹, E. Kido²¹⁴, H. B. Kim²⁰⁹, J. H. Kim²⁰⁷, J. H. Kim²⁰⁷, S. W. Kim²¹⁹, Y. Kimura²⁰⁸, S. Kishigami²⁰⁸, Y. Kubota²¹⁵, S. Kurisu²¹⁵, V. Kuzmin^{221,239}, M. Kuznetsov^{221,224}, Y. J. Kwon²²⁵, K. H. Lee²¹⁹, B. Lubsandorzhev²²¹, K. Machida²¹⁷, H. Matsumiya²⁰⁸, T. Matsuyama²⁰⁸, J. N. Matthews²⁰⁷, R. Mayta²⁰⁸, M. Minamino²⁰⁸, K. Mukai²¹⁷, I. Myers²⁰⁷, S. Nagataki²¹⁴, K. Nakai²⁰⁸, R. Nakamura²¹⁵, T. Nakamura²²⁶, T. Nakamura²¹⁵, Y. Nakamura²¹⁵, A. Nakazawa²¹⁵, E. Nishio²²³, T. Nonaka²¹¹, H. Oda²⁰⁸, S. Ogio^{208,227}, M. Ohnishi²¹¹, H. Ohoka²¹¹, Y. Oku²²³, T. Okuda²²⁸, Y. Omura²⁰⁸, M. Ono²¹⁴, R. Onogi²⁰⁸, A. Oshima²²⁹, S. Ozawa²³⁰, I. H. Park²¹⁹, M. Potts²⁰⁷, M. S. Pshirkov^{221,231}, J. Remington²⁰⁷, D. C. Rodriguez²⁰⁷, G. I. Rubtsov²²¹, D. Ryu²³², H. Sagawa²¹¹, R. Sahara²⁰⁸, Y. Saito²¹⁵, N. Sakaki²¹¹, T. Sako²¹¹, N. Sakurai²⁰⁸, K. Sano²¹⁵, K. Sato²⁰⁸, T. Seki²¹⁵, K. Sekino²¹¹, P. D. Shah²⁰⁷, Y. Shibasaki²¹⁵, F. Shibata²¹⁷, N. Shibata²²³, T. Shibata²¹¹, H. Shimodaira²¹¹, B. K. Shin²³², H. S. Shin²¹¹, D. Shinto²²³, J. D. Smith²⁰⁷, P. Sokolsky²⁰⁷, N. Sone²¹⁵, B. T. Stokes²⁰⁷, T. A. Stroman²⁰⁷, Y. Takagi²⁰⁸, Y. Takahashi²⁰⁸, M. Takamura²¹⁰, M. Takeda²¹¹, R. Takeishi²¹¹, A. Taketa²³³, M. Takita²¹¹, Y. Tameda²²³, H. Tanaka²⁰⁸, K. Tanaka²³⁴, M. Tanaka²³⁵, Y. Tanoue²⁰⁸, S. B. Thomas²⁰⁷, G. B. Thomson²⁰⁷, P. Tinyakov^{221,224}, I. Tkachev²²¹, H. Tokuno²³⁶, T. Tomida²¹⁵, S. Troitsky²²¹, R. Tsuda²⁰⁸, Y. Tsunesada^{208,227}, Y. Uchihori²³⁷, S. Udo²¹⁶, T. Uehama²¹⁵, F. Urban²³⁸, D. Warren²¹⁴, T. Wong²⁰⁷, M. Yamamoto²¹⁵, K. Yamazaki²²⁹, K. Yashiro²¹⁰, F. Yoshida²²³, Y. Yoshioka²¹⁵, Y. Zhezher^{211,221}, and Z. Zundel²⁰⁷

¹ Université de Strasbourg, CNRS, IPHC UMR 7178, F-67000 Strasbourg, France

² Université de Haute Alsace, F-68100 Mulhouse, France

³ IFIC—Instituto de Física Corpuscular (CSIC—Universitat de València) c/ Catedrático José Beltrán, 2 E-46980 Paterna, Valencia, Spain

⁴ Technical University of Catalonia, Laboratory of Applied Bioacoustics, Rambla Exposició, E-08800 Vilanova i la Geltrú, Barcelona, Spain

⁵ INFN—Sezione di Genova, Via Dodecaneso 33, I-16146 Genova, Italy

⁶ Institut d'Investigació per a la Gestió Integrada de les Zones Costaneres (IGIC) - Universitat Politècnica de València. C/ Paranimf 1, E-46730 Gandia, Spain

⁷ Aix Marseille Univ, CNRS/IN2P3, CPPM, Marseille, France

⁸ Université de Paris, CNRS, Astroparticule et Cosmologie, F-75013 Paris, France

⁹ Aix Marseille Univ, CNRS, CNES, LAM, Marseille, France

¹⁰ National Center for Energy Sciences and Nuclear Techniques, B.P.1382, R.P.10001 Rabat, Morocco

¹¹ University Mohammed V in Rabat, Faculty of Sciences, 4 av. Ibn Battouta, B.P. 1014, R.P. 10000, Rabat, Morocco

¹² INFN—Laboratori Nazionali del Sud (LNS), Via S. Sofia 62, I-95123 Catania, Italy

¹³ Friedrich-Alexander-Universität Erlangen-Nürnberg, Erlangen Centre for Astroparticle Physics, Erwin-Rommel-Str. 1, D-91058 Erlangen, Germany

¹⁴ University Mohammed I, Laboratory of Physics of Matter and Radiations, B.P.717, Oujda 6000, Morocco

¹⁵ Nikhef, Science Park, Amsterdam, The Netherlands

¹⁶ Institute of Space Science, RO-077125 Bucharest, Măgurele, Romania

¹⁷ Universiteit van Amsterdam, Instituut voor Hoge-Energie Fysica, Science Park 105, 1098 XG Amsterdam, The Netherlands

¹⁸ INFN—Sezione di Roma, P.le Aldo Moro 2, I-00185 Roma, Italy

¹⁹ Dipartimento di Fisica dell'Università La Sapienza, P.le Aldo Moro 2, I-00185 Roma, Italy

²⁰ LPHEA, Faculty of Science—Semlali, Cadi Ayyad University, P.O.B. 2390, Marrakech, Morocco

²¹ INFN—Sezione di Bologna, Viale Berti-Pichat 6/2, I-40127 Bologna, Italy

²² INFN—Sezione di Bari, Via E. Orabona 4, I-70126 Bari, Italy

²³ Department of Computer Architecture and Technology/CITIC, University of Granada, E-18071 Granada, Spain

²⁴ Université Paris-Sud, F-91405 Orsay Cedex, France

²⁵ Dipartimento di Fisica e Astronomia dell'Università, Viale Berti Pichat 6/2, I-40127 Bologna, Italy

²⁶ Laboratoire de Physique Corpusculaire, Clermont Université, Université Blaise Pascal, CNRS/IN2P3, BP 10448, F-63000 Clermont-Ferrand, France

²⁷ LIS, UMR Université de Toulon, Aix Marseille Université, F-83041 Toulon, France

²⁸ Dipartimento di Fisica dell'Università, Via Dodecaneso 33, I-16146 Genova, Italy

²⁹ Royal Netherlands Institute for Sea Research (NIOZ), Landsdiep 4, 1797 SZ 't Horntje (Texel), The Netherlands

³⁰ Géoazur, UCA, CNRS, IRD, Observatoire de la Côte d'Azur, Sophia Antipolis, France

³¹ International Centre for Radio Astronomy Research—Curtin University, Bentley, WA 6102, Australia

³² Huygens-Kamerlingh Onnes Laboratorium, Universiteit Leiden, The Netherlands

³³ Institut für Theoretische Physik und Astrophysik, Universität Würzburg, Emil-Fischer Str. 31, D-97074 Würzburg, Germany

³⁴ Dr. Remeis-Sternwarte and ECAP, Friedrich-Alexander-Universität Erlangen-Nürnberg, Sternwartstr. 7, D-96049 Bamberg, Germany

³⁵ Mediterranean Institute of Oceanography (MIO), Aix-Marseille University, 13288, Marseille, Cedex 9, France; Université du Sud Toulon-Var, CNRS-INSU/IRD

UM 110, F-83957, La Garde Cedex, France

³⁶ INFN—Sezione di Catania, Via S. Sofia 64, I-95123 Catania, Italy

³⁷ Dpto. de Física Teórica y del Cosmos & C.A.F.P.E., University of Granada, E-18071 Granada, Spain

³⁸ IRFU, CEA, Université Paris-Saclay, F-91191 Gif-sur-Yvette, France

³⁹ INFN—Sezione di Napoli, Via Cintia I-80126 Napoli, Italy
⁴⁰ Museo Storico della Fisica e Centro Studi e Ricerche Enrico Fermi, Piazza del Viminale 1, I-00184, Roma, Italy
⁴¹ INFN—CNAF, Viale C. Berti Pichat 6/2, 40127, Bologna
⁴² Institut Universitaire de France, F-75005 Paris, France
⁴³ Dipartimento di Fisica dell'Università Federico II di Napoli, Via Cintia I-80126, Napoli, Italy
⁴⁴ Department of Physics, Loyola University Chicago, Chicago, IL 60660, USA
⁴⁵ DESY, D-15738 Zeuthen, Germany
⁴⁶ Dept. of Physics and Astronomy, University of Canterbury, Private Bag 4800, Christchurch, New Zealand
⁴⁷ Université Libre de Bruxelles, Science Faculty CP230, B-1050 Brussels, Belgium
⁴⁸ Niels Bohr Institute, University of Copenhagen, DK-2100 Copenhagen, Denmark
⁴⁹ Oskar Klein Centre and Dept. of Physics, Stockholm University, SE-10691 Stockholm, Sweden
⁵⁰ Dept. of Physics, TU Dortmund University, D-44221 Dortmund, Germany
⁵¹ Département de physique nucléaire et corpusculaire, Université de Genève, CH-1211 Genève, Switzerland
⁵² Karlsruhe Institute of Technology, Institute for Astroparticle Physics, D-76021 Karlsruhe, Germany
⁵³ Bartol Research Institute and Dept. of Physics and Astronomy, University of Delaware, Newark, DE 19716, USA
⁵⁴ Department of Physics, Marquette University, Milwaukee, WI 53201, USA
⁵⁵ Dept. of Physics, Pennsylvania State University, University Park, PA 16802, USA
⁵⁶ Erlangen Centre for Astroparticle Physics, Friedrich-Alexander-Universität Erlangen-Nürnberg, D-91058 Erlangen, Germany
⁵⁷ Department of Physics and Laboratory for Particle Physics and Cosmology, Harvard University, Cambridge, MA 02138, USA
⁵⁸ Dept. of Physics and Wisconsin IceCube Particle Astrophysics Center, University of Wisconsin–Madison, Madison, WI 53706, USA; analysis@icecube.wisc.edu
⁵⁹ Dept. of Physics, Massachusetts Institute of Technology, Cambridge, MA 02139, USA
⁶⁰ Physics Department, South Dakota School of Mines and Technology, Rapid City, SD 57701, USA
⁶¹ Dept. of Physics and Astronomy, University of California, Irvine, CA 92697, USA
⁶² Dept. of Physics, University of California, Berkeley, CA 94720, USA
⁶³ Dept. of Astronomy, Ohio State University, Columbus, OH 43210, USA
⁶⁴ Dept. of Physics and Center for Cosmology and Astro-Particle Physics, Ohio State University, Columbus, OH 43210, USA
⁶⁵ Dept. of Physics, University of Wuppertal, D-42119 Wuppertal, Germany
⁶⁶ Fakultät für Physik & Astronomie, Ruhr-Universität Bochum, D-44780 Bochum, Germany
⁶⁷ Physik-department, Technische Universität München, D-85748 Garching, Germany
⁶⁸ Dept. of Physics and Astronomy, University of Rochester, Rochester, NY 14627, USA
⁶⁹ Dept. of Physics, University of Maryland, College Park, MD 20742, USA
⁷⁰ Also at Università di Padova, I-35131 Padova, Italy
⁷¹ Dept. of Physics and Astronomy, University of Kansas, Lawrence, KS 66045, USA
⁷² Lawrence Berkeley National Laboratory, Berkeley, CA 94720, USA
⁷³ III. Physikalisches Institut, RWTH Aachen University, D-52056 Aachen, Germany
⁷⁴ Institute of Physics, University of Mainz, Staudinger Weg 7, D-55099 Mainz, Germany
⁷⁵ Dept. of Physics and Astronomy, Uppsala University, Box 516, SE-75120 Uppsala, Sweden
⁷⁶ School of Physics and Center for Relativistic Astrophysics, Georgia Institute of Technology, Atlanta, GA 30332, USA
⁷⁷ Karlsruhe Institute of Technology, Institute of Experimental Particle Physics, D-76021 Karlsruhe, Germany
⁷⁸ Department of Physics, University of Adelaide, Adelaide, 5005, Australia
⁷⁹ Institut für Kernphysik, Westfälische Wilhelms-Universität Münster, D-48149 Münster, Germany
⁸⁰ Dept. of Physics, Drexel University, 3141 Chestnut Street, Philadelphia, PA 19104, USA
⁸¹ Dept. of Physics and Astronomy, Stony Brook University, Stony Brook, NY 11794-3800, USA
⁸² Dept. of Physics, Sungkyunkwan University, Suwon 16419, Republic of Korea
⁸³ Dept. of Physics and Astronomy, Michigan State University, East Lansing, MI 48824, USA
⁸⁴ Dept. of Physics, Engineering Physics, and Astronomy, Queen's University, Kingston, ON K7L 3N6, Canada
⁸⁵ Vrije Universiteit Brussel (VUB), Dienst ELEM, B-1050 Brussels, Belgium
⁸⁶ Dept. of Astronomy and Astrophysics, Pennsylvania State University, University Park, PA 16802, USA
⁸⁷ Dept. of Physics and Astronomy, University of Alabama, Tuscaloosa, AL 35487, USA
⁸⁸ Centre for Cosmology, Particle Physics and Phenomenology—CP3, Université catholique de Louvain, Louvain-la-Neuve, Belgium
⁸⁹ Institut für Physik, Humboldt-Universität zu Berlin, D-12489 Berlin, Germany
⁹⁰ Dept. of Physics, Southern University, Baton Rouge, LA 70813, USA
⁹¹ Institute of Physics, Academia Sinica, Taipei, 11529, Taiwan
⁹² Dept. of Astronomy, University of Wisconsin–Madison, Madison, WI 53706, USA
⁹³ Dept. of Physics, University of Alberta, Edmonton, AB T6G 2E1, Canada
⁹⁴ Dept. of Physics and Institute for Global Prominent Research, Chiba University, Chiba 263-8522, Japan
⁹⁵ Also at Earthquake Research Institute, University of Tokyo, Bunkyo, Tokyo 113-0032, Japan
⁹⁶ CTSPS, Clark-Atlanta University, Atlanta, GA 30314, USA
⁹⁷ Dept. of Physics, University of Texas at Arlington, 502 Yates St., Science Hall Rm 108, Box 19059, Arlington, TX 76019, USA
⁹⁸ Department of Physics and Astronomy, UCLA, Los Angeles, CA 90095, USA
⁹⁹ Dept. of Physics, Yale University, New Haven, CT 06520, USA
¹⁰⁰ Department of Physics, Mercer University, Macon, GA 31207-0001, USA
¹⁰¹ Dept. of Physics and Astronomy, University of Gent, B-9000 Gent, Belgium
¹⁰² Dept. of Physics and Astronomy, University of Alaska Anchorage, 3211 Providence Dr., Anchorage, AK 99508, USA
¹⁰³ Department of Physics and Astronomy, University of Utah, Salt Lake City, UT 84112, USA
¹⁰⁴ Dept. of Physics, University of Oxford, Parks Road, Oxford OX1 3PU, UK
¹⁰⁵ Dept. of Physics, University of Wisconsin, River Falls, WI 54022, USA
¹⁰⁶ Institute of Basic Science, Sungkyunkwan University, Suwon 16419, Republic of Korea
¹⁰⁷ Laboratório de Instrumentação e Física Experimental de Partículas—LIP and Instituto Superior Técnico—IST, Universidade de Lisboa—UL, Lisboa, Portugal
¹⁰⁸ Osservatorio Astrofisico di Torino (INAF), Torino, Italy
¹⁰⁹ INFN, Sezione di Torino, Torino, Italy
¹¹⁰ University of Adelaide, Adelaide, S.A., Australia
¹¹¹ Centro Atómico Bariloche and Instituto Balseiro (CNEA-UNCuyo-CONICET), San Carlos de Bariloche, Argentina
¹¹² Institute of Nuclear Physics PAN, Krakow, Poland
¹¹³ Instituto de Tecnologías en Detección y Astropartículas (CNEA, CONICET, UNSAM), Buenos Aires, Argentina
¹¹⁴ Universidad Tecnológica Nacional—Facultad Regional Buenos Aires, Buenos Aires, Argentina

¹¹⁵ Instituto Galego de Física de Altas Enerxías (IGFAE), Universidade de Santiago de Compostela, Santiago de Compostela, Spain
¹¹⁶ IMAPP, Radboud University Nijmegen, Nijmegen, The Netherlands
¹¹⁷ Department of Physics and Astronomy, Lehman College, City University of New York, Bronx, NY 10468, USA
¹¹⁸ INFN, Sezione di Napoli, Napoli, Italy
¹¹⁹ RWTH Aachen University, III. Physikalisches Institut A, Aachen, Germany
¹²⁰ Università Torino, Dipartimento di Fisica, Torino, Italy
¹²¹ Universidad Michoacana de San Nicolás de Hidalgo, Morelia, Michoacán, México
¹²² Observatorio Pierre Auger and Comisión Nacional de Energía Atómica, Malargüe, Argentina
¹²³ University Politehnica of Bucharest, Bucharest, Romania
¹²⁴ Institute of Physics of the Czech Academy of Sciences, Prague, Czech Republic
¹²⁵ "Horia Hulubei" National Institute for Physics and Nuclear Engineering, Bucharest-Magurele, Romania
¹²⁶ Gran Sasso Science Institute, L'Aquila, Italy
¹²⁷ INFN Laboratori Nazionali del Gran Sasso, Assergi (L'Aquila), Italy
¹²⁸ Universidad Nacional de San Agustín de Arequipa, Facultad de Ciencias Naturales y Formales, Arequipa, Peru
¹²⁹ Univ. Grenoble Alpes, CNRS, Grenoble Institute of Engineering Univ. Grenoble Alpes, LPSC-IN2P3, F-38000 Grenoble, France
¹³⁰ Max-Planck-Institut für Radioastronomie, Bonn, Germany
¹³¹ Instituto de Física de Rosario (IFIR)—CONICET/U.N.R. and Facultad de Ciencias Bioquímicas y Farmacéuticas U.N.R., Rosario, Argentina
¹³² Karlsruhe Institute of Technology (KIT), Institute for Experimental Particle Physics, Karlsruhe, Germany
¹³³ Université Paris-Saclay, CNRS/IN2P3, IJCLab, Orsay, France
¹³⁴ Karlsruhe Institute of Technology (KIT), Institute for Astroparticle Physics, Karlsruhe, Germany
¹³⁵ Università dell'Aquila, Dipartimento di Scienze Fisiche e Chimiche, L'Aquila, Italy
¹³⁶ International Center of Advanced Studies and Instituto de Ciencias Físicas, ECYT-UNSAM and CONICET, Campus Miguelete—San Martín, Buenos Aires, Argentina
¹³⁷ Universidade Federal do Rio de Janeiro, Instituto de Física, Rio de Janeiro, RJ, Brazil
¹³⁸ Universidade Estadual de Campinas, IFGW, Campinas, SP, Brazil
¹³⁹ Colorado State University, Fort Collins, CO 80521, USA
¹⁴⁰ Universität Siegen, Department Physik—Experimentelle Teilchenphysik, Siegen, Germany
¹⁴¹ Universidad de Granada and C.A.F.P.E., Granada, Spain
¹⁴² Vrije Universiteit Brussels, Brussels, Belgium
¹⁴³ INFN, Sezione di Catania, Catania, Italy
¹⁴⁴ Universidad Autónoma de Chiapas, Tuxtla Gutiérrez, Chiapas, México
¹⁴⁵ Università di Milano, Dipartimento di Fisica, Milano, Italy
¹⁴⁶ INFN, Sezione di Milano, Milano, Italy
¹⁴⁷ Nationaal Instituut voor Kernfysica en Hoge Energie Fysica (NIKHEF), Science Park, Amsterdam, The Netherlands
¹⁴⁸ Bergische Universität Wuppertal, Department of Physics, Wuppertal, Germany
¹⁴⁹ Università di Catania, Dipartimento di Fisica e Astronomia "Ettore Majorana", Catania, Italy
¹⁵⁰ Universidade de São Paulo, Escola de Engenharia de Lorena, Lorena, SP, Brazil
¹⁵¹ INFN, Sezione di Lecce, Lecce, Italy
¹⁵² Observatorio Pierre Auger, Malargüe, Argentina
¹⁵³ Palacky University, RCPTM, Olomouc, Czech Republic
¹⁵⁴ Instituto de Tecnologías en Detección y Astropartículas (CNEA, CONICET, UNSAM), and Universidad Tecnológica Nacional—Facultad Regional Mendoza (CONICET/CNEA), Mendoza, Argentina
¹⁵⁵ Università di Napoli "Federico II" Dipartimento di Fisica "Ettore Pancini", Napoli, Italy
¹⁵⁶ University of Delaware, Department of Physics and Astronomy, Bartol Research Institute, Newark, DE 19716, USA
¹⁵⁷ Politecnico di Milano, Dipartimento di Scienze e Tecnologie Aerospaziali, Milano, Italy
¹⁵⁸ Universidade Federal Fluminense, EEIMVR, Volta Redonda, RJ, Brazil
¹⁵⁹ Case Western Reserve University, Cleveland, OH 44106, USA
¹⁶⁰ Instituto de Astronomía y Física del Espacio (IAFE, CONICET-UBA), Buenos Aires, Argentina
¹⁶¹ Departamento de Física and Departamento de Ciencias de la Atmósfera y los Océanos, FCEyN, Universidad de Buenos Aires and CONICET, Buenos Aires, Argentina
¹⁶² Universidade Federal do Rio de Janeiro (UFRJ), Observatório do Valongo, Rio de Janeiro, RJ, Brazil
¹⁶³ Instituto Federal de Educação, Ciência e Tecnologia do Rio de Janeiro (IFRJ), Brazil
¹⁶⁴ Università del Salento, Dipartimento di Matematica e Fisica "E. De Giorgi", Lecce, Italy
¹⁶⁵ Universidade de São Paulo, Instituto de Física de São Carlos, São Carlos, SP, Brazil
¹⁶⁶ CNRS/IN2P3, IJCLab, Université Paris-Saclay, Orsay, France
¹⁶⁷ Universidad Nacional Autónoma de México, México, D.F., México
¹⁶⁸ Universidade Federal do Paraná, Setor Palotina, Palotina, Brazil
¹⁶⁹ IFLP, Universidad Nacional de La Plata and CONICET, La Plata, Argentina
¹⁷⁰ Fermi National Accelerator Laboratory, Fermilab, Batavia, IL 60510, USA
¹⁷¹ Stichting Astronomisch Onderzoek in Nederland (ASTRON), Dwingeloo, The Netherlands
¹⁷² University of Chicago, Enrico Fermi Institute, Chicago, IL 60637, USA
¹⁷³ New York University, New York, NY 10012, USA
¹⁷⁴ Karlsruhe Institute of Technology (KIT), Institut für Prozessdatenverarbeitung und Elektronik, Karlsruhe, Germany
¹⁷⁵ Michigan Technological University, Houghton, MI 49931, USA
¹⁷⁶ Experimental Particle Physics Department, J. Stefan Institute, Ljubljana, Slovenia
¹⁷⁷ Center for Astrophysics and Cosmology (CAC), University of Nova Gorica, Nova Gorica, Slovenia
¹⁷⁸ Now at Hakubi Center for Advanced Research and Graduate School of Science, Kyoto University, Kyoto, Japan
¹⁷⁹ Université Libre de Bruxelles (ULB), Brussels, Belgium
¹⁸⁰ Universidade Estadual de Feira de Santana, Feira de Santana, Brazil
¹⁸¹ Institute of Space Science, Bucharest-Magurele, Romania
¹⁸² Colorado School of Mines, Golden, CO 80401, USA
¹⁸³ Centro Federal de Educação Tecnológica Celso Suckow da Fonseca, Nova Friburgo, Brazil
¹⁸⁴ Universidade Federal do ABC, Santo André, SP, Brazil
¹⁸⁵ Laboratoire de Physique Nucléaire et de Hautes Energies (LPNHE), Sorbonne Université, Université de Paris, CNRS-IN2P3, Paris, France
¹⁸⁶ Benemérita Universidad Autónoma de Puebla, Puebla, México
¹⁸⁷ University of Wisconsin-Madison, Department of Physics and WIPAC, Madison, WI 53706, USA
¹⁸⁸ Universität Hamburg, II. Institut für Theoretische Physik, Hamburg, Germany
¹⁸⁹ Università di Palermo, Dipartimento di Fisica e Chimica "E. Segrè", Palermo, Italy

¹⁹⁰ Louisiana State University, Baton Rouge, LA 70803, USA
¹⁹¹ Università di Roma “Tor Vergata” Dipartimento di Fisica, Roma, Italy
¹⁹² INFN, Sezione di Roma “Tor Vergata”, Roma, Italy
¹⁹³ Pennsylvania State University, University Park, PA 16802, USA
¹⁹⁴ Centro de Investigaciones en Láseres y Aplicaciones, CITEDEF and CONICET, Villa Martelli, Argentina
¹⁹⁵ Charles University, Faculty of Mathematics and Physics, Institute of Particle and Nuclear Physics, Prague, Czech Republic
¹⁹⁶ Universidad Industrial de Santander, Bucaramanga, Colombia

¹⁹⁷ Unidad Profesional Interdisciplinaria en Ingeniería y Tecnologías Avanzadas del Instituto Politécnico Nacional (UPIITA-IPN), México, D.F., México
¹⁹⁸ Universidade de São Paulo, Instituto de Física, São Paulo, SP, Brazil
¹⁹⁹ Istituto di Astrofisica Spaziale e Fisica Cosmica di Palermo (INAF), Palermo, Italy
²⁰⁰ Centro Brasileiro de Pesquisas Físicas, Rio de Janeiro, RJ, Brazil
²⁰¹ Also at University of Bucharest, Physics Department, Bucharest, Romania
²⁰² University of Łódź, Faculty of High-Energy Astrophysics, Łódź, Poland
²⁰³ Universidad de Medellín, Medellín, Colombia
²⁰⁴ Universiteit van Amsterdam, Faculty of Science, Amsterdam, The Netherlands
²⁰⁵ School of Physics and Astronomy, University of Leeds, Leeds, UK
²⁰⁶ Department of Physics, Loyola University Chicago, Chicago, IL 60611, USA
²⁰⁷ High Energy Astrophysics Institute and Department of Physics and Astronomy, University of Utah, Salt Lake City, UT 84112, USA
²⁰⁸ Graduate School of Science, Osaka City University, Osaka, Osaka, Japan
²⁰⁹ Department of Physics and The Research Institute of Natural Science, Hanyang University, Seongdong-gu, Seoul, Republic of Korea
²¹⁰ Department of Physics, Tokyo University of Science, Noda, Chiba, Japan
²¹¹ Institute for Cosmic Ray Research, University of Tokyo, Kashiwa, Chiba, Japan
²¹² Currently at University of California—Santa Cruz, CA 95064, USA
²¹³ Currently at Flatiron Institute, Simons Foundation, NY 10010, USA
²¹⁴ Astrophysical Big Bang Laboratory, RIKEN, Wako, Saitama, Japan

²¹⁵ Academic Assembly School of Science and Technology Institute of Engineering, Shinshu University, Nagano, Nagano, Japan
²¹⁶ Faculty of Engineering, Kanagawa University, Yokohama, Kanagawa, Japan
²¹⁷ Interdisciplinary Graduate School of Medicine and Engineering, University of Yamanashi, Kofu, Yamanashi, Japan
²¹⁸ The Graduate School of Science and Engineering, Saitama University, Saitama, Saitama, Japan
²¹⁹ Department of Physics, SungKyunKwan University, Jang-an-gu, Suwon, Republic of Korea
²²⁰ Department of Physics, Tokyo City University, Setagaya-ku, Tokyo, Japan
²²¹ Institute for Nuclear Research of the Russian Academy of Sciences, Moscow, Russia
²²² Faculty of Systems Engineering and Science, Shibaura Institute of Technology, Minato-ku, Tokyo, Japan
²²³ Department of Engineering Science, Faculty of Engineering, Osaka Electro-Communication University, Neyagawa-shi, Osaka, Japan
²²⁴ Service de Physique Théorique, Université Libre de Bruxelles, Brussels, Belgium
²²⁵ Department of Physics, Yonsei University, Seodaemun-gu, Seoul, Republic of Korea
²²⁶ Faculty of Science, Kochi University, Kochi, Kochi, Japan
²²⁷ Nambu Yoichiro Institute of Theoretical and Experimental Physics, Osaka City University, Osaka, Osaka, Japan
²²⁸ Department of Physical Sciences, Ritsumeikan University, Kusatsu, Shiga, Japan
²²⁹ College of Engineering, Chubu University, Kasugai, Aichi, Japan

²³⁰ Quantum ICT Advanced Development Center, National Institute for Information and Communications Technology, Koganei, Tokyo, Japan
²³¹ Sternberg Astronomical Institute, Moscow M.V. Lomonosov State University, Moscow, Russia
²³² Department of Physics, School of Natural Sciences, Ulsan National Institute of Science and Technology, UNIST-gil, Ulsan, Republic of Korea
²³³ Earthquake Research Institute, University of Tokyo, Bunkyo-ku, Tokyo, Japan
²³⁴ Graduate School of Information Sciences, Hiroshima City University, Hiroshima, Hiroshima, Japan
²³⁵ Institute of Particle and Nuclear Studies, KEK, Tsukuba, Ibaraki, Japan
²³⁶ Graduate School of Science and Engineering, Tokyo Institute of Technology, Meguro, Tokyo, Japan
²³⁷ Department of Research Planning and Promotion, Quantum Medical Science Directorate, National Institutes for Quantum and Radiological Science and Technology, Chiba, Chiba, Japan
²³⁸ CEICO, Institute of Physics, Czech Academy of Sciences, Prague, Czech Republic

Received 2022 January 31; revised 2022 April 12; accepted 2022 May 5; published 2022 August 3

Abstract

For several decades, the origin of ultra-high-energy cosmic rays (UHECRs) has been an unsolved question of high-energy astrophysics. One approach for solving this puzzle is to correlate UHECRs with high-energy neutrinos, since neutrinos are a direct probe of hadronic interactions of cosmic rays and are not deflected by magnetic fields. In this paper, we present three different approaches for correlating the arrival directions of neutrinos with the arrival directions of UHECRs. The neutrino data are provided by the IceCube Neutrino Observatory and ANTARES, while the UHECR data with energies above ~ 50 EeV are provided by the Pierre Auger Observatory and the Telescope Array. All experiments provide increased statistics and improved reconstructions with respect to our previous results reported in 2015. The first analysis uses a high-statistics neutrino sample optimized for point-source searches to search for excesses of neutrino clustering in the vicinity of UHECR directions. The second analysis searches for an excess of UHECRs in the direction of the highest-energy neutrinos. The third analysis searches for an excess of pairs of UHECRs and highest-energy neutrinos

²³⁹ Deceased.

 Original content from this work may be used under the terms of the [Creative Commons Attribution 4.0 licence](#). Any further distribution of this work must maintain attribution to the author(s) and the title of the work, journal citation and DOI.

on different angular scales. None of the analyses have found a significant excess, and previously reported overfluctuations are reduced in significance. Based on these results, we further constrain the neutrino flux spatially correlated with UHECRs.

Key words: Neutrino astronomy – High energy astrophysics – Ultra-high-energy cosmic radiation

1. Introduction

Earth is continuously bombarded by high-energy cosmic rays, most of which are charged atomic nuclei (Particle Data Group et al. 2020). It is generally believed that cosmic rays with energies above 1 EeV (10^{18} eV), known as ultra-high-energy cosmic rays (UHECRs), mostly originate from extragalactic sources in the nearby universe. Based on the estimated magnitude of galactic magnetic fields (Nagano & Watson 2000), cosmic rays below this energy are believed to diffuse within their host galaxy, whereas cosmic rays above this energy escape from the galaxy. These assumptions are confirmed by the observation of large-scale anisotropies in the arrival directions of UHECRs above 8 EeV with the excess flux directed from outside of our Galaxy (Aab et al. 2017). The two largest observatories for UHECRs are the Pierre Auger Observatory (Auger; The Pierre Auger Collaboration 2015) in Argentina in the Southern Hemisphere and the Telescope Array (TA; Abu-Zayyad et al. 2012) in the United States in the Northern Hemisphere. They have performed detailed analyses of the arrival directions of detected UHECRs and have revealed interesting features, such as possible correlations with the directions of known starburst and active galaxies in the nearby universe observed by Auger (Aab et al. 2018; Biteau et al. 2022), and intermediate-scale directional clustering observed by TA (Abbasi et al. 2014; Tkachev et al. 2021). However, due to the small number of events detected at the highest energies, these indications of anisotropic arrival directions have not yet been confirmed on the 5σ level. Thus, neither Auger nor TA reports an unambiguous identification of the UHECR sources to date. One of the main reasons is the deflection of cosmic rays by magnetic fields during propagation from their sources to Earth, which alters their directional information with respect to the source positions. The deflection of UHECRs increases with increasing charge, which is not well determined at the highest energies above 50 EeV considered in this work. This uncertainty additionally complicates the identification of UHECR sources. Nevertheless, UHECRs at the highest energies are deflected the least owing to their extremely high magnetic rigidity (Alves Batista et al. 2019), which makes them suitable for directional correlation searches.

We search for the sources of the highest-energy cosmic rays with a multimessenger approach using high-energy neutrinos and UHECRs with energies above ~ 50 EeV. High-energy neutrinos are direct tracers of hadronic interactions of cosmic rays and are thus expected to be produced at the acceleration site or during propagation (see, e.g., Murase 2015; Mészáros 2018; Anchordoqui et al. 2008). Furthermore, the electrically neutral neutrinos carry the directional information of their origin, since they are not deflected by magnetic fields. A combined analysis of UHECRs and high-energy neutrinos is further motivated by the observation of a diffuse flux of high-energy neutrinos of astrophysical origin above the background of atmospheric neutrinos. The flux follows a hard power law that extends to energies of multiple PeV and possibly beyond (The IceCube Collaboration 2013; Aartsen et al. 2016; Stettner 2019; Aartsen et al. 2020d; Abbasi et al. 2021). The measured flux is closely below the Waxman–Bahcall bound (Waxman & Bahcall 1999; Bahcall & Waxman 2001), which is

a theoretical upper bound on the astrophysical neutrino flux derived from the observed UHECR flux, suggesting a connection between UHECRs and high-energy neutrinos (Murase et al. 2013; Ahlers & Halzen 2018). We note that the Seyfert and starburst galaxy NGC 1068 appears both as a neutrino source candidate in Aartsen et al. (2020c) and as a UHECR source candidate in Aab et al. (2018). Recently, the potential of high-energy neutrinos in a multimessenger approach has been demonstrated together with observations of high-energy photons (Aartsen et al. 2018b, 2018c), finding compelling evidence for neutrino emission from the blazar TXS 0506+056. At the same time, it can be concluded that blazars seem insufficient to saturate the total observed neutrino flux (Murase & Waxman 2016; Aartsen et al. 2017a) based on the nonobservation of steady neutrino fluxes from known blazars in the universe. This result motivates different approaches to identify hadronic sources in the local universe; a promising method is to correlate the sources traced with UHECRs with high-energy neutrinos, and vice versa.

In this paper, we report results from three conceptually different approaches. All are based on correlating the arrival directions of high-energy neutrinos detected by the IceCube Neutrino Observatory (IC; Aartsen et al. 2017d) and the ANTARES experiment (ANT; Ageron et al. 2011) with the arrival directions of UHECRs with energies above ~ 50 EeV measured by Auger and TA:

1. Analysis 1 (described in Section 4.1) uses the measured UHECR directions, as well as magnetic deflection estimates, for identifying regions in which we search for point-like neutrino sources.
2. Analysis 2 (described in Section 4.2) uses the arrival directions of neutrinos with a high probability of astrophysical origin to search for a correlated clustering of UHECR arrival directions, while also accounting for the magnetic deflection.
3. Analysis 3 (described in Section 4.3) is based on a largely model-independent two-point correlation analysis of the arrival directions of UHECRs and neutrinos with a high probability of astrophysical origin.

With these three approaches, we follow up on previous searches performed by the Pierre Auger, Telescope Array, and IceCube Collaborations (The IceCube Collaboration et al. 2016), which showed an interesting correlation at a significance level close to three standard deviations.

Since 2015, the analyses have been improved with substantially enlarged data sets, extending the Auger data from 10 to 13 yr (see Section 2.3) and TA data from 6 to 9 yr (see Section 2.4). The different data sets from IceCube are enlarged from 4 to 10.5 yr, from 4 to 7.5 yr, and from 2 to 8 yr, depending on the specific detection channel as described in Section 2.1. Newly included are two data sets of 9 and 11 yr from ANTARES, as further specified in Section 2.2. Due to the updated data sets by Auger and TA, their respective shift of the energy scale is updated from a sole shift of TA energies by -13% to a shift of $+14\%$ for Auger and -14% TA energies

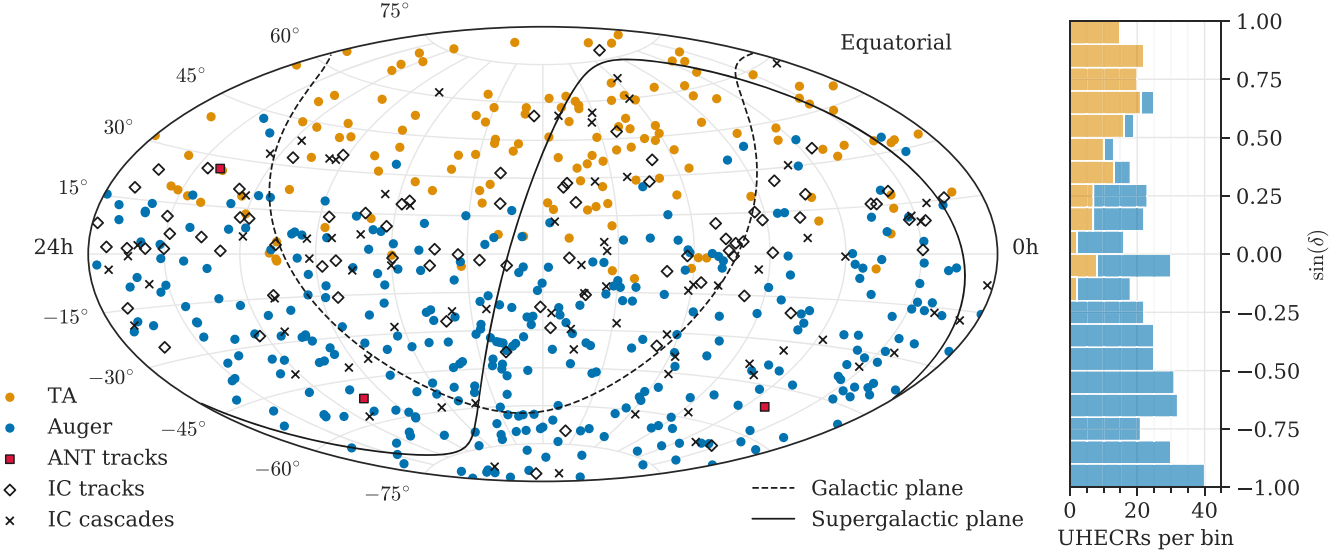


Figure 1. Left: sky map of the arrival directions of UHECR events and high-energy neutrinos. The high-energy neutrino track-like events from IceCube consist of the HESE, HENU, and EHE data sets, while the cascade-like events are only of the IceCube-HESE data sets. From ANTARES, only high-energy tracks are selected for the analyses. Right: histogram of the decl. of UHECR events, separated into Auger and TA contributions.

above the energy threshold of ~ 50 EeV (Biteau et al. 2019). Furthermore, we include an improved magnetic deflection model that distinguishes between the Northern and Southern Hemispheres for analysis 2. We report the results from the three improved correlation searches, which update the preliminary reported results in Schumacher (2019), Aublin et al. (2019), and Barbano (2019). In addition, we report upper limits on the correlated fluxes of UHECRs and neutrinos based on benchmark models for the magnetic deflections.

2. Observatories and Data Sets

All data sets used in this paper are used in previous work by the four respective collaborations. This section focuses on the main aspects relevant for our analyses.

2.1. The IceCube Neutrino Observatory

The IceCube Neutrino Observatory (Aartsen et al. 2017d) is an ice-Cherenkov detector sensitive to neutrinos with energies ≥ 5 GeV. It is located at the geographic South Pole, about 1.45–2.45 km deep in the ice. Its main component consists of a volume of about 1 km^3 glacial ice instrumented with 5160 photomultipliers that are connected to the surface by 86 cable strings.

Two classes of neutrino-induced events can be phenomenologically distinguished: elongated, track-like events that are produced by muons that originate mostly from charged-current ν_μ interactions; and the spherical, cascade-like events that originate from charged-current ν_e and ν_τ interactions with hadronic and electromagnetic decays, as well as neutral-current interactions of all flavors. Typically, track-like events enable a better angular resolution than cascade-like events owing to their different topologies, but they provide a poorer energy resolution (Aartsen et al. 2014a; Wandkowsky 2018). One method of suppressing the dominant background of down-going muons produced by cosmic-ray interactions in the atmosphere is by selecting events with the interaction vertex within the detector (Aartsen et al. 2014c; Kopper 2017; Wandkowsky 2018). Alternatively, through-going tracks with either horizontal or up-going directions are selected, such that

the atmospheric muons are blocked out by Earth (Aartsen et al. 2016; Haack & Wiebusch 2017). In the case of down-going tracks, a high-energy threshold and elaborate selection procedures are necessary to filter out atmospheric muons (Aartsen et al. 2017b, 2017c, 2018c). In all cases, the remaining event rate is dominated by atmospheric neutrinos. The selection of astrophysical neutrinos can be achieved on a statistical basis by selecting very energetic events or, in the case of the very down-going region, by vetoing events where an atmospheric shower is observed in IceTop, IceCube’s surface detector for cosmic rays (Abbasi et al. 2013).

For the three analyses, data from multiple detection channels are used, which are (i) a data set of through-going tracks from the full sky optimized for point-source searches (PS), (ii) a data set of high-energy starting events (HESE) of both topologies from the full sky, (iii) a data set of high-energy neutrinos (HENU) selected from through-going tracks with horizontal and up-going directions, and (iv) a data set of tracks from a selection of extremely high energy events (EHE). The PS data set is used for analysis 1, while the HESE, HENU, and EHE data sets are used for analyses 2 and 3. For analyses 2 and 3, track-like events from the HESE, HENU, and EHE data sets are combined, while multiple instances of identical events are removed. This results in a data set of 81 track-like events. In analyses 2 and 3, the 76 cascade-like events from the HESE data set are analyzed separately owing to their larger directional uncertainty. The sky distribution of selected events is shown in Figure 1, and an overview of the nomenclature is presented in Table 1.

The PS data set consists of a combination of data collected from 7 yr of operation between 2008 and 2015 that were used for point-source searches (Aartsen et al. 2017b) and data from 3.5 yr of operation between 2015 and 2018 that were selected for the real-time gamma-ray follow-up (GFU) program of IceCube (Aartsen et al. 2017c, 2018c). The combined data set consists of about 1.4 million track-like events above ~ 100 GeV. It is dominated by atmospheric neutrinos in the Northern Hemisphere and by atmospheric muons in the Southern Hemisphere. The median of the angular resolution (Ψ) is better than 0.5° above energies of a few TeV. Figure 2 shows the

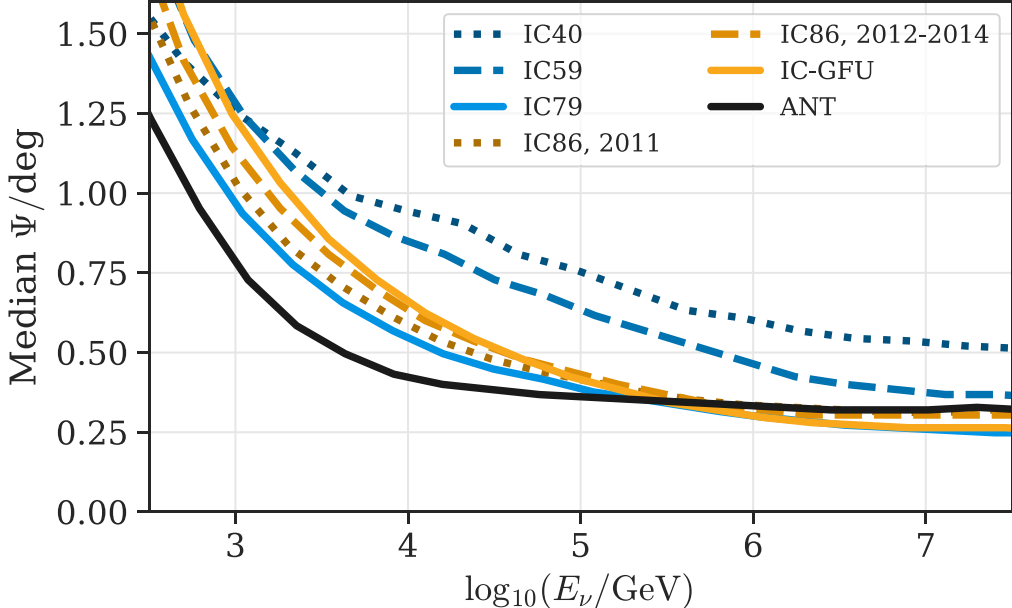


Figure 2. Median of the angular resolution, Ψ , which is the angle between the true neutrino direction and reconstructed muon direction for IceCube and ANTARES point-source data as a function of the true neutrino energy. This is calculated based on simulation data sets. The data from partial detector configurations of IceCube are denoted by the number of operating strings (IC40, IC59, IC79; Aartsen et al. 2014b) and are shown in blue. The data of the full detector configuration with 86 strings, including the GFU data set (Aartsen et al. 2017b, 2017c, 2018c), are identified by the years of data taking and are shown in orange. The angular resolution of ANTARES data for the 11 yr data set (Albert et al. 2018; Illuminati et al. 2019) is shown in black.

Table 1
Overview of Different Neutrino Data Sets Used in the Different Analyses

Detector	Analysis 1	Analysis 2	Analysis 3
ANTARES	PS	HENU	HENU
IceCube	PS	HESE + HENU + EHE	HESE + HENU + EHE
<hr/>			
Data set	Description		Topology
PS	Optimized for point-source searches, ν_μ candidates		Tracks
HESE	High-energy starting events, all flavors		Tracks and cascades
HENU	High-energy selection of ν_μ candidates		Tracks
EHE	Extremely high energy ν_μ candidates		Tracks

median of the angular resolution for the different detector configurations of IceCube and for data from the ANTARES detector (see Section 2.2). Note that analysis 1 is based not on the median of the angular resolution but on the estimator for the angular resolution on an event-by-event basis (σ).

The HESE data set contains 76 cascade-like events and 26 track-like events that have been collected between 2010 and 2017, as presented in Wandkowsky (2018). It consists of neutrinos of all flavors that interacted inside the detection volume, called starting events, with deposited energies ranging between about 20 TeV and 2 PeV. Integrated above 60 TeV, which corresponds to 60 events in total, the percentage of events of astrophysical origin, i.e., the astrophysical purity, is larger than 75% (Wandkowsky 2018), while the percentage is lower below 60 TeV. The angular resolution is about 1° for track-like events and 15° for cascade-like events above 100 TeV. The resolution of the deposited energy for tracks and cascades is around 10% (Aartsen et al. 2014a) without accounting for systematic uncertainties, but the cascades have a

better correlation with the primary neutrino energy since they deposit most of their energy inside the detector, while tracks do not.

The HENU data set consists of the 35 highest-energy track-like events with a reconstructed decl. $\geq -5^\circ$, which have been collected between 2009 and 2016 (Haack & Wiebusch 2017) for the measurement of the diffuse muon–neutrino flux (Aartsen et al. 2016). From the original data set starting at ~ 100 GeV, only events of high probability of nonatmospheric origin have been selected by applying an energy threshold of ≥ 200 TeV on the reconstructed muon energy. This corresponds to an astrophysical purity of more than 50%. The astrophysical purity here is defined as the flux ratio of the astrophysical to the sum of atmospheric and astrophysical differential fluxes and thus depends on the assumed astrophysical flux. For the estimation of the astrophysical purity, the best-fit astrophysical flux from Aartsen et al. (2016), $d\phi/dE = 1.01 \times 10^{18} \text{ GeV}^{-1} \text{ cm}^{-2} \text{ s}^{-1} \text{ sr}^{-1} (E/100 \text{ TeV})^{-2.19}$, is used, as well as the best-fit atmospheric flux from the same reference.

The EHE data set consists of 20 events that have been collected between 2008 and 2017 (Aartsen et al. 2017c, 2018a). The selection is targeting high-energy track-like events of good angular resolution $\leq 1^\circ$. The selection has been optimized to be sensitive to events in the energy range of 0.5–10.0 PeV. The integrated astrophysical purity depends on the assumption on the spectrum of astrophysical events at the highest energies but can be estimated as approximately 60% purity (see Table 2 in Aartsen et al. 2017c).

2.2. The ANTARES Neutrino Telescope

The ANTARES telescope (Ageron et al. 2011) is a deep-sea Cherenkov neutrino detector located 40 km offshore from Toulon, France, in the Mediterranean Sea. The detector is composed of 12 vertical strings anchored at the sea floor at a depth of 2475 m. The strings are spaced at distances of about 70 m from each other, instrumenting a total volume of $\sim 0.01 \text{ km}^3$. Each string is equipped with 25 storeys of three optical modules (ANTARES Collaboration et al. 2002), vertically spaced by 14.5 m, for a total of 885 optical modules. Each optical module houses a 10-inch photomultiplier tube facing 45° downward to optimize the detection of light from upward-going charged particles. The detector was completed in 2008.

The ANTARES and IceCube detection principles are very similar (see Section 2.1). Particles above the Cherenkov threshold induce coherent radiation emitted in a cone with a characteristic angle of 42° in water. The position, time, and collected charge of the signals induced in the photomultiplier tubes by detected photons are used to reconstruct the direction and energy of events induced by neutrino interactions and atmospheric muons. Trigger conditions based on combinations of local coincidences are applied to identify signals due to physics events over the environmental light background due to ^{40}K decays and bioluminescence (Aguilar et al. 2007). ANTARES is thus also capable of detecting charged–current and neutral–current neutrino interactions of all flavors.

For analysis 1, we use all track-like events from the 11 yr data set used for point-source searches (PS) recorded between 2007 and 2017 (Albert et al. 2018; Illuminati et al. 2019). The high-energy events (HENU) for analyses 2 and 3 are selected from an earlier data set of track-like and cascade-like events collected between 2007 and 2015 (Albert et al. 2017). In order to ensure a high probability of astrophysical origin for analyses 2 and 3, we require an astrophysical purity $\geq 40\%$ based on the same definition as used for the HENU data set of IceCube. This selection results in a total of three track-like events and no cascade-like events, of which the arrival directions are shown in Figure 1. An overview of the nomenclature is presented in Table 1. The track-like events are combined with the respective IceCube data sets. All events have a good angular resolution that is below 0.4° above 10 TeV (Albert et al. 2017). Overall, the angular resolution of ANTARES tracks is better than for IceCube tracks for energies below 100 TeV and comparable around 100 TeV and above. The median angular resolution, Ψ , of the 11 yr data set compared to the IceCube PS data set is shown in Figure 2.

Despite the smaller detection volume, the inclusion of ANTARES data significantly improves the all-sky coverage of the neutrino data set used in analysis 1. This is shown in Section 4.1 and Figure 5 through the relative contribution to the expected number of signal events for the individual PS data

sets of ANTARES and IceCube. Particularly in the Southern Hemisphere, where the background from atmospheric muons results in a higher energy threshold in IceCube, the ANTARES data contribute substantially to the signal acceptance for soft source spectra.

2.3. The Pierre Auger Observatory

The Pierre Auger Observatory is located in Argentina (32° S , 69° W) at a mean altitude of 1.4 km above sea level (The Pierre Auger Collaboration 2015). The observatory has a hybrid design combining an array of particle detectors at ground (surface detector, SD) and an atmospheric fluorescence detector (FD) for detecting the air showers caused by UHECRs interacting with the atmosphere. The SD array is composed of 1660 water-Cherenkov detectors spread over an area of 3000 km^2 . The SD area is overlooked by the FD, which consists of 27 wide-angle optical telescopes located at four sites. The reconstruction of SD events is described in detail in Aab et al. (2020b). The energy estimate is based on the signal at 1000 m from the reconstructed intersection of the shower axis with the ground, which is extracted with a fit of the lateral distribution of signals in the individual detectors. This value is then corrected to take into account the different absorption suffered by showers coming at different angles. Due to the hybrid design of the observatory, this energy estimator is calibrated via the correlation with the near-calorimetric energy measured by the FD with the events observed by both SD and FD. Through this calibration, the energy estimate for SD is done without relying on Monte Carlo. At the energies considered in this work, the systematic uncertainty on the energy scale is 14% (Dawson 2019), the statistical uncertainty on the energy due to the number of triggered SD stations and uncertainties of their response is smaller than 12% (Abreu et al. 2011; Aab et al. 2020b), and the angular uncertainty is less than 0.9° (Bonifazi & The Pierre Auger Collaboration 2009).

The UHECR data set used here consists of 324 events observed with the SD between 2004 January and 2017 April (Aab et al. 2018) with reconstructed energies $\geq 52 \text{ EeV}$ and zenith angles $\leq 80^\circ$. The data statistics is enlarged with respect to the previously used data set (Aab et al. 2015) by 93 events and includes an updated energy calibration based on a larger number of hybrid events and an improved absorption correction. The angular acceptance translates into a field of view ranging from -90° to 45° in decl. All energies are scaled up by a constant factor of 14% to match both Auger and TA energies on a common energy scale (see Section 2.4), following the recommendation of the Auger–TA joint working group (Biteau et al. 2019). This scaling factor was determined by cross-calibrating the measured UHECR fluxes in the declination band around the celestial equator covered by both observatories. It is chosen such that the fluxes in the common declination band match at 40 EeV of the Auger data set and at 53 EeV of the TA data set, respectively. The celestial distribution of the UHECR arrival directions is shown in Figure 1. The directional exposure as a function of decl. can be found in Figure 3, which amounts to an integrated geometric exposure of $91,300 \text{ km}^2 \text{ yr sr}$.

2.4. The Telescope Array

The TA is located in Millard County, Utah, USA (39.3° N , 112.9° W) at an altitude of about 1.4 km (Kawai et al. 2008). It

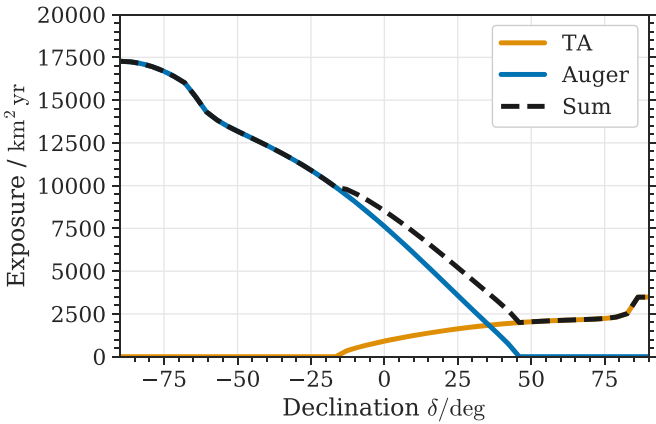


Figure 3. Directional exposures of TA, Auger, and their sum. The underlying geometric exposure functions are derived from Sommers (2001). See also Figure 1 of Biteau et al. (2019).

consists of a surface detector (SD) array, composed of 507 plastic scintillation detectors of 3 m^2 each. The SD stations are located on a square grid with 1.2 km separation, which extends over an area of 700 km^2 (Abu-Zayyad et al. 2012). The TA SD array observes UHECRs with a duty cycle near 100%. With its wide field of view, the SD array covers a range from -15° to 90° in decl. In addition to the SD, there are three fluorescence telescope stations, instrumented with 12–14 telescopes each (Tokuno et al. 2012). The telescope stations observe the sky above the SD array and measure the longitudinal development of the air showers as they traverse the atmosphere.

The data set for this analysis follows the selection in Abbasi et al. (2014), which has been updated to 9 yr of data in Abbasi et al. (2018). The data set is identical to the data set used for anisotropy analyses presented in Troitsky et al. (2017). It consists of 143 events observed with the SD between 2008 May and 2017 May with reconstructed energies $\geq 57\text{ EeV}$ and zenith angles $\leq 55^\circ$. At these energies, the angular uncertainty is about 1.5° . The statistical uncertainty on the reconstructed energy is about 15%–20%, with an additional systematic uncertainty on the energy scale of 21% (Abbasi et al. 2018). All energies are scaled down by -14% to match both Auger and TA energies on a common energy scale (see Section 2.3), following the recommendation of the Auger–TA joint working group (Biteau et al. 2019).

The celestial distribution of selected events is shown in Figure 1. The right-hand side of the figure is a histogram of the sine of decl. of all UHECR events, showing that TA data substantially contributes to the full-sky exposure of the combined UHECR data set. Figure 3 shows the directional exposure as a function of decl., with an integrated total exposure of $11,600\text{ km}^2\text{ yr sr}$ (Biteau et al. 2019).

3. Magnetic Deflections

Despite their extremely high rigidity, UHECRs are deflected in galactic and in extragalactic magnetic fields (GMF/EGMF) by a nonnegligible amount. Neither the strength and correlation length of the extragalactic magnetic fields (Durrer & Neronov 2013; Kronberg 1994) nor the distances of the UHECR sources are known well. Measurements of the Faraday rotation of extragalactic sources indicate that the extragalactic magnetic fields are weaker than 1 nG (Pshirkov et al. 2016). Assuming a correlation length of $\sim 1\text{ Mpc}$, this results in a deflection less than 2° for protons of 100 EeV , even at source distances of

50 Mpc. In line with the previously reported results (The IceCube Collaboration et al. 2016), the deflection outside of our Galaxy is assumed to be generally weaker than within our Galaxy, and it is not modeled explicitly but benchmarked within the uncertainty of the deflection by GMF and the uncertainty of the rigidity due to the unknown composition.

The measurement and modeling of the GMF is a complex task and the subject of ongoing discussion.²⁴⁰ Among different proposed models, we use the JF2012 (Jansson & Farrar 2012) model and the PT2011 (Pshirkov et al. 2011) model to estimate the deflection of the UHECRs in the GMF. Both models consist of a disk and a halo component, while the JF2012 model has an additional X-shaped field component perpendicular to the disk. A propagation simulation has been conducted with a Monte Carlo approach to estimate the deflection of protons with an energy of 100 EeV that are distributed isotropically outside of the GMF. The resulting deflections are shown in Figure 4, split into the Galactic northern and southern hemispheres based on the arrival direction of the proton. The estimated deflection shows a complex structure that differs considerably for the two models. However, the mean deflection is about 3° in both cases. Due to the heavy tails of the distributions, the mean is consistently larger than the median; thus, we choose the mean as a conservative deflection estimate. The split into the two hemispheres shows a considerably smaller deflection in the Galactic north than in the Galactic south owing to north–south asymmetries present in both models of the GMF. For this work we have chosen a robust benchmark modeling of the effect of the GMF, thus avoiding biases of detailed model uncertainties. The deflection process is assumed to be random, resulting in a symmetric 2D Gaussian distribution of UHECR arrival directions around a given source direction. In reverse, the source position is assumed to be located within the 2D Gaussian distribution around the arrival direction of a UHECR event. The standard deviation of the Gaussian deflection, σ_{MD} , depends on a scaling factor, C , and inversely on the energy of the UHECR event, E_{CR} ,

$$\sigma_{\text{MD}} = \frac{D_0 \cdot C}{E_{\text{CR}}/100\text{ EeV}}. \quad (1)$$

The default deflection, D_0 , for $C = 1$ and $E_{\text{CR}} = 100\text{ EeV}$ is derived from the mean of the deflection values obtained with the simulation, which are shown in Figure 4. Note that the deflection is usually a 2D quantity with (x, y) coordinates, which in Figure 4 is projected to the absolute value, i.e., $\sqrt{x^2 + y^2}$. Furthermore, larger and thus more conservative values of the deflection will be tested to include an uncertainty of the GMF model. The scaling factor C thus accounts for uncertainties of both GMF model and UHECR charge, which is not known on an event-by-event basis at highest energies.

Analysis 1 uses a default deflection of $D_0 = 3^\circ$ over the whole sky, while analysis 2 uses $D_{\text{North/South}} = (2.4^\circ, 3.7^\circ)$ for UHECRs with arrival directions from the Galactic northern and southern hemispheres, respectively. The different choices have been made based on the respectively better sensitivity for the two analyses. Analyses 1 and 2 implement the deflection into their methods as described in the respective Sections 4.1 and 4.2. Analysis 3 employs a model-independent approach with respect to the UHECR deflection.

²⁴⁰ See <https://icrc2021-venue.desy.de> for a recent review by Tess Jaffe on the GMF at ICRC2021: “Constraining Magnetic Fields at Galactic Scales”.

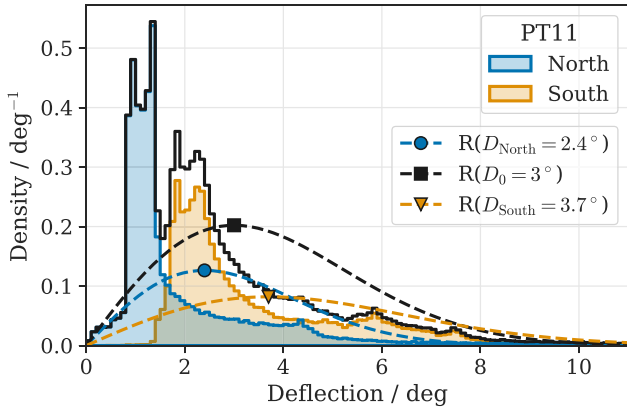


Figure 4. Deflection simulation for protons of 100 EeV and two different galactic magnetic models: PT2011 (Pshirkov et al. 2011) and JF2012 (Jansson & Farrar 2012). Shaded areas in blue and orange show the histogram split into Galactic northern and southern hemispheres, respectively, with their sum shown as a black line. Additionally, Rayleigh pdfs are shown in the same colors; a Rayleigh function with mode σ is the 1D projection of a symmetric 2D Gaussian function with width σ , with the projection being $(x, y) \rightarrow \sqrt{x^2 + y^2}$. The position of the markers indicate the mode of the Rayleigh pdf and thus the value of the default deflection, D . Note that the integrals of the split pdfs are normalized to 0.5, while the integrals of the full pdfs are normalized to 1.

4. Analysis Methods

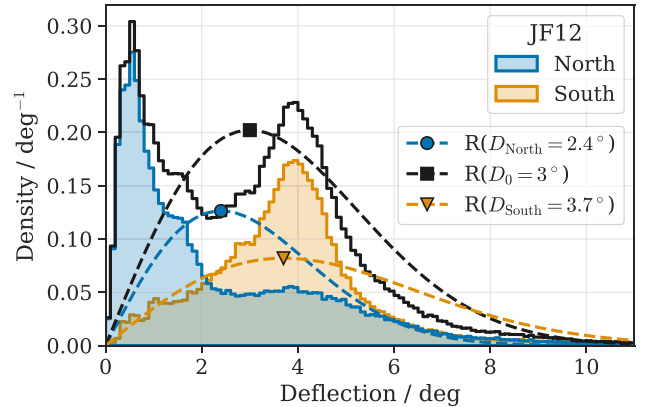
4.1. Unbinned Neutrino Point-source Search with UHECR Information

The goal of analysis 1 is to find point-like neutrino sources that are spatially correlated with UHECR arrival directions within a region derived from their magnetic deflection estimate. The search for neutrino sources utilizes the unbinned maximum likelihood analysis commonly used in IceCube (Aartsen et al. 2017b, 2019, 2020c). This enables an easy combination of the high-statistics, full-sky neutrino data sets, which are the PS data sets of IceCube and ANTARES described in Sections 2.1 and 2.2, respectively. In addition to this standard method, the magnetic deflection regions, defined by the UHECR arrival directions, energy, and scaling factor, are used for constraining the possible source regions.

The unbinned neutrino likelihood in the source direction $\vec{\Omega} = (\alpha, \delta)$ in R.A. and decl. consists of the sum of a signal probability density function (pdf), S , and a background pdf, B ,

$$\mathcal{L}(n_s, \gamma) = \prod_{j=1}^7 \prod_{i=1}^{N_j} f_j(\sin \delta, \gamma) \frac{n_s}{N_j} \cdot S(\vec{\Omega}_i, E_i, \sigma_i | \gamma, \vec{\Omega}) + \left(1 - f_j(\sin \delta, \gamma) \frac{n_s}{N_j}\right) \cdot B(\delta_i, E_i). \quad (2)$$

The likelihood product with index i runs over all neutrino events within each data set with index j (see Sections 2.1 and 2.2). The likelihood product with index j runs over all data sets to yield the final likelihood function. The likelihood combination of the seven data sets by ANTARES and IceCube is thus handled the same way as described in Aartsen et al. (2017b). The signal and background pdfs, S and B , are evaluated for four observables per neutrino event, weighted with the number of signal events over total number of events per data set, n_s/N_j . The observables are the reconstructed R.A. and decl., summarized as $\vec{\Omega}_i = (\alpha_i, \delta_i)$, reconstructed energy, E_i , and angular error estimator, σ_i . The signal pdf consists of two terms: the first term is a decl.-dependent reconstructed energy



distribution, where the underlying neutrino flux is modeled as a power law,

$$\frac{d\Phi^\nu}{dE} = \frac{dN^\nu}{dE dA dt d\Omega} = \Phi_0^\nu \cdot \left(\frac{E}{1 \text{ GeV}}\right)^{-\gamma}. \quad (3)$$

Here Φ_0^ν is the flux normalization, 1 GeV is the corresponding pivot energy, and γ is the spectral index of the power law. The second term of the signal pdf is a spatial term modeled as a Gaussian, with the width, σ_i , given by the angular error estimator of each neutrino candidate on an event-by-event basis. The background pdf is determined as a function of reconstructed energy, E_i , and decl., δ_i , from randomized experimental data. A full description of the signal and background pdfs, S and B , can be found in Aartsen et al. (2017b). The proportionality factor, $f_j(\sin \delta, \gamma)$, is the relative signal acceptance per neutrino data set calculated from the expected number of signal events via

$$f_j(\sin \delta, \gamma) = \frac{n_j}{n_{\text{tot}}} = \frac{T^j \int (d\Phi^\nu/dE) A_{\text{eff}}^j(E, \sin \delta) dE}{\sum_{j=1}^7 T^j \int (d\Phi^\nu/dE) A_{\text{eff}}^j(E, \sin \delta) dE}. \quad (4)$$

This factor is used to correctly weight the signal contribution of each data set j for a given source decl. and spectral index. Per data set j , the live time is denoted with T^j and the effective area is denoted with A_{eff}^j . Figure 5 shows the proportionality factor of each data set as a function of decl. for two spectral indices, $\gamma = 2.0$ and 2.5 . Note that all data sets are evaluated with the same formulation of the likelihood function as used by IceCube, instead of combining different formulations as described in Albert et al. (2020).

The best-fit signal parameters, \hat{n}_s and $\hat{\gamma}$, at a given source position, $\vec{\Omega}$, are obtained with the maximum likelihood method. The number of events and the proportionality factor are related to the neutrino flux using the respective live time and effective

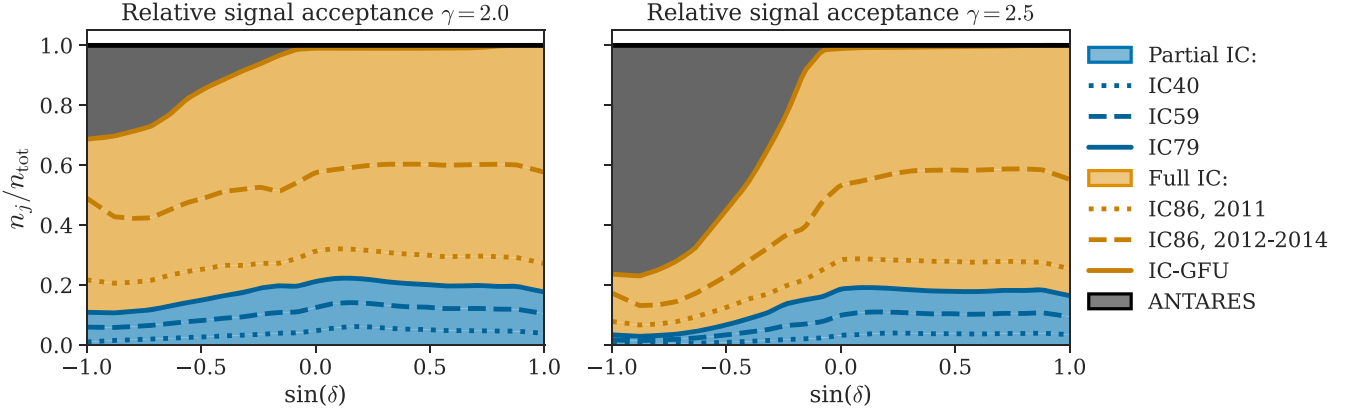


Figure 5. The relative signal contribution, n_j/n_{tot} , for analysis 1 of the different configurations of IceCube and the ANTARES point-source data set as a function of the decl. δ . The left panel shows a hard underlying power-law signal spectrum (Equation (3)) with index $\gamma = 2.0$, while the right panel shows a softer spectrum with $\gamma = 2.5$. The relative signal contributions from partial detector configurations of IceCube are shown in blue, while the contributions of the full detector configuration of IceCube with 86 strings are shown in orange. The ANTARES contribution is shown in gray. The lines as listed in the rightmost legend indicate the contributions from each data set individually.

area of each data set via

$$n_s = \sum_{j=1}^7 T^j \int \frac{d\Phi^\nu}{dE} A_{\text{eff}}^j(E, \sin \delta) dE. \quad (5)$$

The corresponding significance of a source at position $\vec{\Omega}$ is evaluated using a likelihood ratio test, which yields the test statistic (TS)

$$\text{TS}_\nu(\vec{\Omega}) = 2 \log \left(\frac{\mathcal{L}(\hat{n}_s, \hat{\gamma})}{\mathcal{L}(n_s = 0)} \right) \Bigg|_{\vec{\Omega}}. \quad (6)$$

Here the null hypothesis is defined via $n_s = 0$, representing the case of no neutrino sources in the vicinity of UHECR events. Instead of searching for a single neutrino source, the whole sky is searched on a HEALpix (Górski et al. 2005) grid with a resolution of approximately 0.2° . This results in a sky map of the TS values at each grid center, $\vec{\Omega}_{\text{grid}}$.

The second step is to combine the neutrino likelihood with the information provided by UHECR events and their deflection estimate. The deflection estimate for one UHECR with index k and arrival direction $\vec{\Omega}_k^{\text{CR}}$, which possibly originated in the direction of $\vec{\Omega}_{\text{grid}}$, is defined as a 2D Gaussian. Its width is the quadratic sum of the magnetic deflection estimate, σ_{MD} of Equation (1), and the UHECR angular reconstruction error, σ_{CR}^2 , which is 0.9° for Auger events and 1.5° for TA events,

$$\mathcal{P}_k \propto \exp \left(-\frac{(\vec{\Omega}_{\text{grid}} - \vec{\Omega}_k^{\text{CR}})^2}{2(\sigma_{\text{MD}}^2 + \sigma_{\text{CR}}^2)} \right). \quad (7)$$

The term \mathcal{P}_k acts as a spatial constraint, which is multiplied by the neutrino likelihood function defined in Equation (2) via $\mathcal{L} \rightarrow \mathcal{L} \cdot \mathcal{P}_k$. Effectively, the constraint is added as a logarithmic term to the neutrino TS defined for each grid point in Equation (6) via $\text{TS} \rightarrow \text{TS} + 2 \cdot \log(\mathcal{P}_k)$. Finally, the maximum of the combined UHECR–neutrino TS is found at the best-fit grid point, $\hat{\vec{\Omega}}_{\text{grid}}$, via

$$\text{TS}_k^{\text{comb}}(\hat{\vec{\Omega}}_{\text{grid}}) = \max \left(\text{TS}_\nu(\vec{\Omega}_{\text{grid}}) - \frac{(\vec{\Omega}_{\text{grid}} - \vec{\Omega}_k^{\text{CR}})^2}{\sigma_{\text{MD}}^2 + \sigma_{\text{CR}}^2} \right). \quad (8)$$

The maximum marks the neutrino source candidate that is the most likely counterpart to the respective UHECR event used to calculate the spatial constraint. The normalization in Equation (7) adds only a constant term to the TS, which can be omitted when calculating significances and p -values based on pseudo-experiments (see below). As a third, final step, this procedure is repeated for all UHECRs, and all obtained TS values are added up, yielding the final test statistic. This search strategy was first developed in the context of this point-source correlation analysis and first outlined in Section 4 of Schumacher (2019). It has already been applied also to other neutrino correlation searches with spatially extended source localization, namely, the correlation with ANITA events (Aartsen et al. 2020a) and with gravitational wave events (Aartsen et al. 2020b). Note that the analysis described here is improved with respect to the previous search (The IceCube Collaboration et al. 2016, Section 5), as it models the displacement of a point-like neutrino source with respect to the UHECR arrival direction based on the assumed magnetic deflection. Here the position and flux of a point-like source are fit in the vicinity of the UHECR direction, while in the previous search a spatially extended neutrino emission around the UHECR direction was fit.

Six different signal hypotheses are tested, which are characterized by a lower cut on the UHECR energy, $E_{\text{CR}} > E_{\text{cut}}$ with $E_{\text{cut}} \in \{70, 85, 100\}$ EeV, and the scaling factor of the deflection estimate, $C \in \{1, 2\}$. The lower energy cut is a threshold for selecting only the highest-energy UHECRs with the lowest deflection for this analysis. No analogous energy cut is applied to the neutrino data. The scaling factor C is a model parameter for scaling the baseline magnetic deflection, and it is not derived from the UHECR data. The baseline magnetic deflection is $D_0 = 3^\circ$ for all UHECRs, which is then converted into the spatial constraint of an individual UHECR event using Equations (1) and (7). The corresponding sensitivity and 3σ -discovery potential are evaluated based on the normalization of the neutrino flux per source, Φ_0^ν (see Equation (3)). The 3σ threshold is chosen since the background expectation needs to be calculated based on pseudo-experiments, as described in the next paragraph. A 5σ -discovery potential is computationally too expensive to be calculated for the various hypotheses. Sensitivity is defined as

Table 2

Sensitivity, Discovery Potential, and 90% C.L. Upper Limit for the Different Analysis Parameters, Which Are The UHECR Energy Cut, E_{cut} , Magnetic Deflection, $D_0 \cdot C$, and Correlation Fraction, f_{corr} , for the Point-source Correlation Analysis

Magnetic deflection, $D_0 \cdot C$	3°	3°	3°	6°	6°	6°
Energy cut, E_{cut}	70 EeV	85 EeV	100 EeV	70 EeV	85 EeV	100 EeV
Number of neutrino sources, N_{ν}^{src}						
$f_{\text{corr}} = 0.1$	22	9	4	22	9	4
$f_{\text{corr}} = 0.5$	106	41	20	106	41	20
$f_{\text{corr}} = 1$	211	82	40	211	82	40
Sensitivity						
$f_{\text{corr}} = 0.1$	5.6	7.1	9.8	5.4	8.5	9.5
$f_{\text{corr}} = 0.5$	2.4	2.6	3.1	2.6	3.4	4.2
$f_{\text{corr}} = 1$	1.4	1.7	2.1	1.8	2.2	2.9
3σ disc. potential						
$f_{\text{corr}} = 0.1$	7.2	8.5	11.6	6.7	8.0	10.8
$f_{\text{corr}} = 0.5$	3.7	3.8	4.9	3.7	4.1	5.1
$f_{\text{corr}} = 1$	2.6	2.6	3.2	2.7	3.1	3.7
90% C.L. upper limit						
$f_{\text{corr}} = 0.1$	6.4	9.2	9.8	6.7	10.9	10.6
$f_{\text{corr}} = 0.5$	2.8	3.6	3.1	3.3	4.7	4.5
$f_{\text{corr}} = 1$	1.7	2.3	2.1	2.3	3.2	3.1
Pretrial p-value	0.33	0.23	>0.5	0.19	0.097	0.43

Note. The values of sensitivity, discovery potential, and limit are given as normalization of the neutrino flux per source in units of $10^{-10} \text{ GeV}^{-1} \text{ cm}^{-2} \text{ s}^{-1}$. The neutrino flux per source is modeled with a power law of the form $d\Phi/dE = \Phi_0 \cdot (E/1 \text{ GeV})^{-2}$. The last row states all six experimentally obtained pretrial p -values with respect to the null hypothesis of an isotropic neutrino flux.

the expected median upper limit at 90% confidence level on Φ_0^{ν} in the case of a null measurement, while the discovery potential is defined as the median of Φ_0^{ν} required for a rejection of the background hypothesis with 3σ significance.

Both sensitivity and discovery potential are calculated based on data challenges, for which signal-like and background-like pseudo-experiments (PEs) are generated. Since the calculation is based on PEs, the constant term in Equations (7) and (8), i.e., the normalization of the constraint term, can be omitted. For all signal and background PEs, the UHECR arrival directions are kept fixed. The background PEs are obtained by randomizing the experimental neutrino data in R.A. The signal PEs reflect the six different signal hypotheses; one signal PE is based on experimental neutrino data randomized in R.A., to which Monte Carlo neutrino events, representing a neutrino source, are added. The location of this neutrino source is chosen randomly within the spatial deflection constraint of one UHECR event. This way, we mimic a neutrino source that is displaced with respect to the UHECR direction owing to the UHECR deflection. In the baseline model of the signal PEs, all UHECR events have such an artificial neutrino source in their vicinity. For one PE, all neutrino sources have an E^{-2} power-law spectrum and the same flux normalization. Note that the UHECR energy cut and scaling factor used to generate the spatial constraints for the likelihood function are the same as for determining the neutrino source location.

We generate additional signal PEs by varying the fraction of UHECR events, f_{corr} , with a neutrino source in their vicinity. This mimics signal models where not all UHECRs have a corresponding neutrino source in the vicinity of their arrival direction. Thus, the number of neutrino sources is determined by the rounded-up product of the correlation fraction with the numbers of UHECRs, $N_{\nu}^{\text{src}} = [f_{\text{corr}} N_{\text{CR}}]$, where N_{CR} is the number of UHECRs passing the energy cut. We choose the correlation

fraction from three discrete values, $f_{\text{corr}} \in \{1, 0.5, 0.1\}$, where $f_{\text{corr}} = 1$ represents the baseline model. Note that the correlation fraction is only used to choose the number of neutrino sources in the signal PEs, while in real experimental data it is not known a priori which UHECRs have a correlated neutrino source and which do not. For $f_{\text{corr}} < 1$, only a number $N_{\nu}^{\text{src}} < N_{\text{CR}}$ of randomly selected UHECRs will have a correlated neutrino source in the signal PEs. Independent of the correlation fraction, the TS values of all UHECR constraints are added up, since in real experimental data it would not be known which UHECRs have a correlated neutrino source. The sensitivity and 3σ -discovery potential in terms of the flux normalization per neutrino source for all signal models and hypotheses are reported in Table 2 and also shown in Figure 6. We see that a smaller correlation fraction increases the flux normalization per neutrino source for both sensitivity and 3σ -discovery potential. This is expected since a smaller correlation fraction corresponds to fewer neutrino sources, which in turn need to have a higher flux normalization to be detected by the analysis.

It is noticeable that for a small correlation fraction of $f_{\text{corr}} = 0.1$, the signal model with a larger scaling factor of $C = 2$ yields a better 3σ -discovery potential than the smaller scaling factor of $C = 1$. This is unexpected, as a smaller UHECR deflection and thus a smaller spatial constraint should yield more accuracy in detecting the corresponding neutrino sources. However, the amount of sky covered by the constraints does not grow uniformly with the scaling factor and numbers of UHECRs, since the UHECR spatial constraints can overlap. In the case of a small correlation fraction, a high neutrino flux per source is required to reach the 3σ -discovery potential owing to the small number of sources present.²⁴¹ A

²⁴¹ There are 22, 9, and 4 sources for $f_{\text{corr}} = 0.1$ and the energy cuts of $E_{\text{cut}} \in \{70, 85, 100\}$ EeV, respectively.

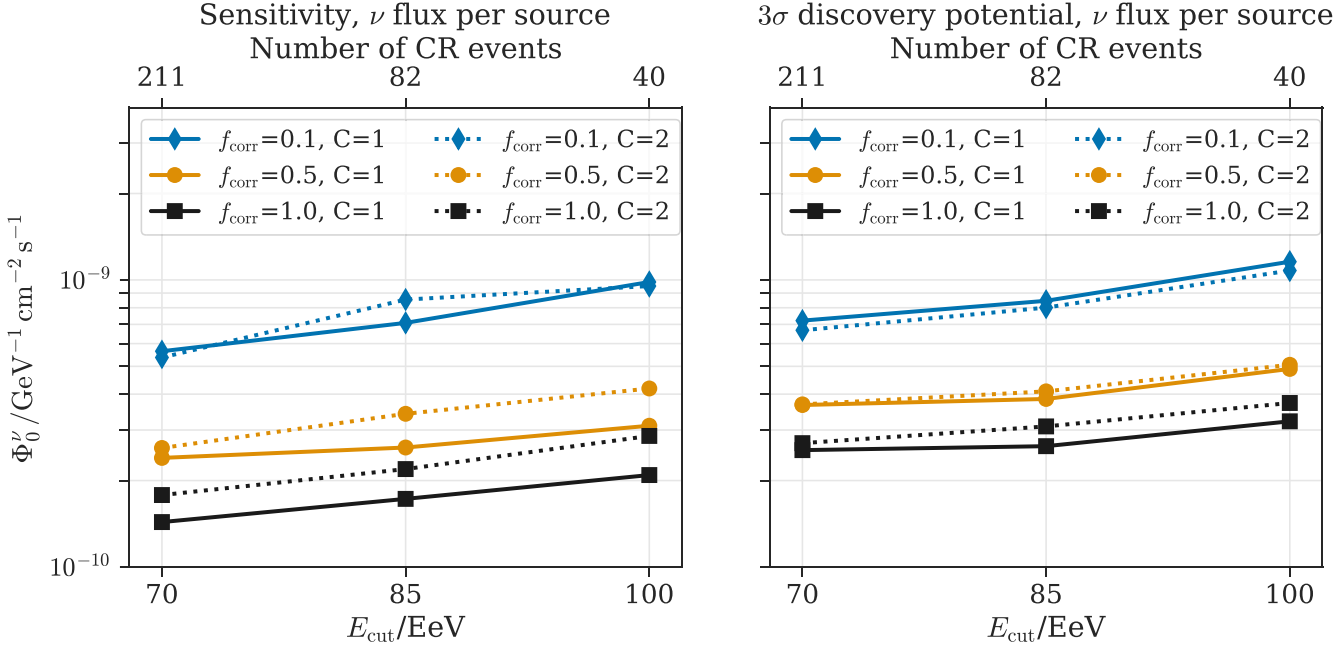


Figure 6. Sensitivity (left) and 3σ -discovery potential (right) of the neutrino flux per source as a function of the UHECR energy cut in EeV, for the three correlation fractions and for the two scaling factors we used.

closer study showed that in the case of few, but strong, neutrino sources, it is beneficial to search a larger area of the sky for sources so that fewer of them are missed. This effect is thus caused by an interplay between deflection size, number of UHECRs, and relatively high neutrino flux per source in this particular case.

4.2. Unbinned Likelihood-stacking Analysis of UHECRs and High-energy Neutrinos

The second analysis is based on using the neutrinos with a high probability of astrophysical origin as markers for the location of the sources of UHECRs and neutrinos. The UHECR events are stacked using an unbinned likelihood analysis with the arrival directions of the high-energy neutrinos as the source positions. The signal hypothesis is defined by the number of UHECR events, which are clustered around the neutrino arrival directions, as well as the size of the magnetic deflection. The background hypothesis is defined by an isotropic flux of UHECRs. This approach is thus complementary to the point-source correlation analysis, where the UHECR events are used as source markers and an isotropic flux of neutrinos defines the background hypothesis. The logarithm of the likelihood function is defined as

$$\log \mathcal{L}(n_s) = \sum_{i=1}^{N_{\text{Auger}}} \log \left(\frac{n_s}{N_{\text{CR}}} S_{\text{Auger}}^i + \frac{N_{\text{CR}} - n_s}{N_{\text{CR}}} B_{\text{Auger}}^i \right) + \sum_{i=1}^{N_{\text{TA}}} \log \left(\frac{n_s}{N_{\text{CR}}} S_{\text{TA}}^i + \frac{N_{\text{CR}} - n_s}{N_{\text{CR}}} B_{\text{TA}}^i \right), \quad (9)$$

where the free parameter is the total number of UHECR signal events, n_s . The sums run over all UHECR events in the respective data set, i.e., N_{Auger} and N_{TA} , where the total number of UHECR events is $N_{\text{CR}} = N_{\text{Auger}} + N_{\text{TA}}$. In contrast to the likelihood function of analysis 1, the signal pdfs, S_{Auger}^i and S_{TA}^i , and the background pdfs, B_{Auger}^i and B_{TA}^i , are stacked for all

high-energy neutrinos such that n_s is a global parameter. The background pdfs per UHECR detector, B_{det}^i , are the normalized expectations for an isotropic UHECR flux as a function of decl., which correspond to the normalized detector exposures (see Figure 3). The signal pdf per UHECR detector is defined as

$$S_{\text{det}}^i(\vec{\Omega}_i, E_i) = R_{\text{det}}(\delta_i) \cdot \sum_{j=1}^{N_{\nu}} S_j(\vec{\Omega}_i, \sigma(E_i)) \quad \text{with } \sigma^2 = \sigma_{\text{MD}}^2 + \sigma_{\text{CR}}^2, \quad (10)$$

as a function of the UHECR arrival direction, $\vec{\Omega}_i$, and energy, E_i . The term R_{det} is the relative exposure of each detector as a function of the decl. per UHECR event, δ_i . Figure 3 shows the absolute directional exposures, which are each normalized to 1 over the whole sky to obtain R_{det} . The sum runs over all neutrino events, N_{ν} , where the terms of $S_j(\vec{\Omega}_i, \sigma(E_i))$ are the spatial likelihood maps obtained from the neutrino directional reconstruction smeared with the UHECR uncertainty with width $\sigma(E_i)$ (see Equation (7)). Thus, these terms are pdfs representing the total uncertainty on the common source position of UHECR event i and neutrino event j , evaluated at the UHECR arrival direction, $\vec{\Omega}_i$. Similar to analysis 1, three different deflections corresponding to scaling factors of $C \in \{1, 2, 3\}$ are represented in the signal terms of the likelihood function. Again, C is a model parameter that scales the magnitude of the deflection and it is not derived from UHECR data. Depending on whether the UHECR arrival direction is in the Galactic northern hemisphere or southern hemisphere (see Figure 4), the baseline magnetic deflection is thus

$$D = C \cdot (D_{\text{North}}, D_{\text{South}}) = C \cdot (2.4, 3.7) \text{ with } C \in \{1, 2, 3\}. \quad (11)$$

The final value of the deflection, σ_{MD} , is then calculated based on the UHECR energy using Equation (1).

Table 3

Sensitivity, 3σ Discovery Potential, and 90% C.L. Upper Limits in Terms of Number of UHECRs (n_s ; see Equation (9)), as well as the Pretrial p -values for the UHECR Stacking Analysis with the Samples of High-energy Tracks and Cascades Assuming an Isotropic Flux of UHECRs

Analysis parameters	(2°.4, 3°.7)	(4°.8, 7°.4)	(7°.2, 11°1)
$D_{N/S} \cdot C$			
Sensitivity			
tracks	9.8	9.8	10.3
cascades	57	61	64
3σ disc. potential			
tracks	20	21	21
cascades	113	129	135
90% C.L. upper limit			
tracks	9.8	9.8	10.3
cascades	55	76	101
Pretrial p -values			
tracks	>0.5	>0.5	>0.5
cascades	>0.5	0.38	0.26

The best fit of the number of signal events, \hat{n}_s , is found with a maximum likelihood estimation. The resulting test statistic is defined as the likelihood ratio of the maximum likelihood over the background likelihood with $n_s = 0$,

$$TS = 2 \log \frac{\mathcal{L}(\hat{n}_s)}{\mathcal{L}(n_s = 0)}. \quad (12)$$

The significance is then determined based on the assumption that the background expectation is distributed according to a χ^2 function with 1 degree of freedom, which has been verified using background-like PEs. The test statistic is calculated separately for all track-like and all cascade-like neutrino events and separately for the three different deflections. The analysis approach is essentially the same as published in The IceCube Collaboration et al. (2016), except for the updated magnetic deflection values, which are split into the Galactic northern and southern hemispheres as described in Section 3.

The sensitivity and the 3σ -discovery potential in terms of n_s are obtained with data challenges based on PEs. Here the neutrino arrival directions are kept fixed per PE, while the UHECR arrival directions and energies are generated resembling the signal and background hypothesis. For the background PEs, all UHECR arrival directions are derived from an isotropic flux and thus according to the exposure of the respective UHECR experiments. The energies of the UHECR events are sampled from a power law proportional to $E^{-4.2}$ for the Auger events and to $E^{-4.5}$ for the TA events, as in The IceCube Collaboration et al. (2016). For the signal PEs, a number n_s of UHECR arrival directions are distributed randomly based on their respective spatial signal terms in Equation (10), $S_j(\Omega_i, \sigma(E_i))$. Note that all UHECRs have the same scaling factor, corresponding to the respective signal hypothesis as implemented in the likelihood function. The sensitivity and 3σ -discovery potential for the three different benchmark values of C are presented in Table 3, separately for the track-like and cascade-like neutrino events. We find that the sensitivity and 3σ -discovery potential using neutrino tracks require much fewer UHECRs than when using neutrino cascades, which is expected owing to the large differences in angular reconstruction uncertainty of the two event topologies.

4.3. Two-point Angular Correlation of UHECRs and High-energy Neutrinos

The 2pt-correlation analysis relies on counting pairs of UHECRs and the high-energy neutrinos, where the angular separation between their arrival directions is within a maximum angular separation, α . The observed number of pairs within this radius, $n_{\text{obs}}(\alpha)$, is compared to the mean number of pairs expected from pure background, i.e., uncorrelated arrival directions, $\langle n_{\text{bckg}}(\alpha) \rangle$. The relative excess of pairs is defined as

$$\frac{n_{\text{obs}}(\alpha)}{\langle n_{\text{bckg}}(\alpha) \rangle} - 1. \quad (13)$$

As the separation angle is not known a priori, angles between 1° and 30° in steps of 1° are tested. The angle with the largest deviation from the background expectation is chosen after the scan.

The significance of the experimental result is calculated with respect to background PEs. Similar to analysis 2, the background PEs are generated with a fixed set of neutrino arrival directions, and uncorrelated UHECR arrival directions are generated according to the exposure of the respective UHECR experiments. The energies are sampled from the same spectra as described in Section 4.2. As a cross-check, additional background PEs are generated with the fixed set of UHECR arrival directions, and neutrino arrival directions are randomized in R.A. The different types of background PEs approximate an isotropic flux of UHECRs and high-energy neutrinos, respectively.

Note that this analysis does not include an assumption of the magnetic deflection of UHECRs, which makes it a robust and model-independent approach. The analysis approach is the same as published in The IceCube Collaboration et al. (2016).

5. Results

5.1. Unbinned Neutrino Point-source Search with UHECR Information

The test statistic of experimental data is obtained with the neutrino point-source correlation analysis as described in Section 4.1, assuming the six different combinations of signal parameters, i.e., combinations of scaling factor, C , and lower energy cut, E_{cut} . Each of the six experimental TS values is evaluated with respect to the corresponding distribution of TS obtained from background-like PEs. The resulting p -values for all six tests are listed in Table 2. The smallest p -value (9.7%) is found for the scaling factor of $C = 2$ and an UHECR energy cut of $E_{\text{cut}} = 85$ EeV. The p -value increases to 24% when correcting for the trials due to the six correlated tests. This correction is based on the combined distribution of all minimum p -values of the background PEs. All p -values are fully compatible with the background hypothesis of no resolved neutrino sources in spatial correlation with the UHECRs considering the assumed signal models. Based on the experimental TS value, 90% C.L. upper limits on the normalization of the flux of neutrino sources correlated with UHECR arrival directions are reported in the last three rows of Table 2. In the case of the single p -value larger than 50% found for $C = 1$ and $E_{\text{cut}} = 100$ EeV, the limits are set equal to the sensitivity in order to not overestimate the limits based on an underfluctuation in data. In addition to the baseline correlation fraction of 100%, the limits are calculated for two smaller

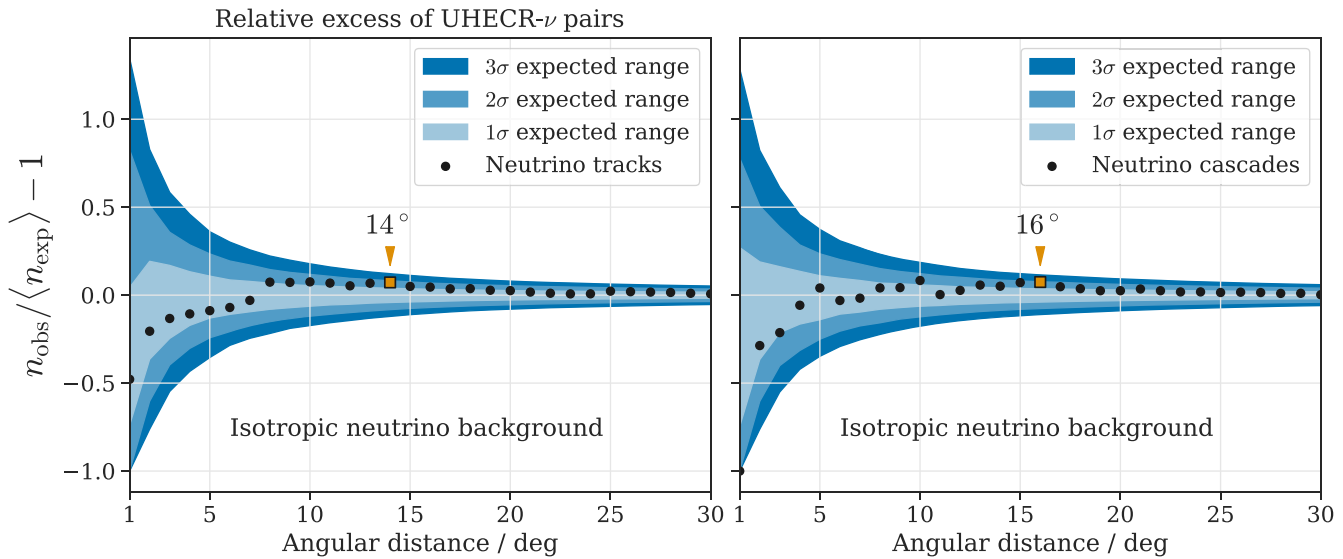


Figure 7. Relative excess of pairs, $n_{\text{obs}} / \langle n_{\text{exp}} \rangle - 1$, as a function of the maximum angular separation of the neutrino and UHECR pairs. The experimental result is shown as black circles, while the blue color bands show the regions containing the 1σ , 2σ , and 3σ fluctuations from background PEs based on an isotropic distribution of high-energy neutrinos. The results for the track-like neutrinos are shown on the left and for the cascade-like neutrino on the right.

Table 4

Posttrial p -value and Best-fit Angular Separation for the 2pt-correlation Analysis Obtained with the Neutrino Data Sets of High-energy Tracks and Cascades, as Stated in the First Column

Event Type	Background Hypothesis	Separation	Posttrial p -value
Tracks	isotropic neutrinos	14°	0.23
Cascades	isotropic neutrinos	16°	0.15
Tracks	isotropic UHECRs	10°	>0.5
Cascades	isotropic UHECRs	16°	0.18

Note. The p -values are corrected for choosing the largest deviation out of all maximum angular separations. The respective background hypotheses are stated in the second column.

correlation fractions of 50% and 10%. In these cases, the limits are relaxed by about 40%–60% for $f_{\text{corr}} = 0.5$ compared to $f_{\text{corr}} = 1$ and by about a factor of 3 to almost 5 for $f_{\text{corr}} = 0.1$ compared to $f_{\text{corr}} = 1$.

5.2. Unbinned Likelihood-stacking Analysis of UHECRs and High-energy Neutrinos

The UHECR stacking analysis is performed for track-like and cascade-like high-energy neutrinos separately for three different scaling factors of $C \in \{1, 2, 3\}$. This results in six p -values with respect to the background hypothesis of an isotropic flux of UHECRs, of which none is significant. The smallest p -value is 0.26, which is found for cascades and the largest scaling factor of $C = 3$, corresponding to the benchmark deflection in the Galactic northern and southern hemispheres of ($7.2^\circ, 11.1^\circ$). Based on the observed TS values, 90% C.L. limits on the number of UHECR events correlated to the high-energy neutrinos are calculated using the PEs of the corresponding signal hypothesis for each of the six tests. Since all p -values using the track-like neutrinos are larger than 0.5, the limits are set equal to the sensitivity in order to not overestimate the limits based on an underfluctuation in data. All p -values and the corresponding limits are reported in Table 3, together with the sensitivity and discovery potential.

5.3. Two-point Angular Correlation of UHECRs and High-energy Neutrinos

The 2pt-correlation analysis is applied to the sets of neutrino tracks and cascades separately, as well as for the background hypothesis of an isotropic UHECRs flux and an isotropic high-energy neutrino flux. The significance of the result with respect to the background hypothesis is corrected for the scan over the separation angles. This results in four p -values and four respective best-fit angular separations, as listed in Table 4. The largest deviation from an isotropic flux of high-energy neutrinos (p -value = 15%) is found using cascades and a maximum angular separation of 16° . None of the p -values show a significant result; thus, the results are all compatible with their respective background hypothesis. The relative excesses of pairs with respect to an isotropic distribution of neutrinos as a function of the separation angle are shown in Figure 7, separately for neutrino tracks and cascades.

6. Conclusions

Three complementary analyses have been performed on the UHECR data sets provided by the Pierre Auger and the Telescope Array Collaborations combined with the high-energy and full-sky neutrino data sets provided by the IceCube and ANTARES Collaborations. For both the UHECR and neutrino data sets, the combination of data from the two respective observatories provides a field of view over the entire sky. None of the analyses found a result incompatible with the assumed background hypotheses of either an isotropic neutrino flux or an isotropic UHECR flux. This is an important update on the results reported in The IceCube Collaboration et al. (2016), where p -values close to the 3σ level were reported when applying analyses 2 and 3 to cascade-like neutrino events.

Based on the results, 90% C.L. upper limits are calculated for analysis 1 on the flux of neutrinos from point-like sources correlated with UHECRs and for analysis 2 on the number of UHECR events correlated with high-energy neutrinos. Analysis 1 reports upper limits on the correlated neutrino flux per

source given different sets of parameters that make assumptions about the lower cut on the UHECR energy and the fraction of UHECRs with a correlated neutrino source, as well as about a scaling factor of the magnetic deflection (see Table 2). Analysis 2 reports upper limits on the number of correlated UHECR events with either track-like or cascade-like neutrinos depending on the scaling factor of the magnetic deflection (see Table 3). This is the first time that upper limits from a direct correlation search of UHECRs and neutrinos are reported.

These limits are calculated based on the assumed signal and background hypotheses and are thus based on the parameters of the respective signal models. In the following, we discuss the limitations of these signal models in the light of underlying assumptions made for the neutrino–UHECR correlation. There are several plausible explanations why we have not observed a significant correlation of UHECRs and neutrinos.

Neutrino sources are presumably distributed over the whole universe, and the emitted neutrinos are able to reach Earth without deflection or absorption. For example, the first neutrino source identified with compelling evidence, TXS 0506+056 (Aartsen et al. 2018b, 2018c), is located at a redshift of $z = 0.34$ (Paiano et al. 2018), corresponding to a comoving distance of about 1.3 Gpc. This is beyond the assumed horizon for UHECR sources in the local universe of up to about 200 Mpc. Therefore, the fraction of correlated sources within the UHECR horizon is small compared to the total number of neutrino sources. This was quantified by Palladino et al. (2020) for muon neutrinos above 200 TeV based on the non-observation of neutrino multiplets above this energy. They concluded that the high-energy flux measured with IceCube must come from a large number of sources such that no multiplets are observed. Necessarily, most of the neutrino sources lie beyond the UHECR horizon, which is used in Palladino et al. (2020) to explain the lack of UHECR–neutrino correlations found in The IceCube Collaboration et al. (2016) and Schumacher (2019), and the same applies to the current study. In these studies, however, the energy threshold for neutrinos lies around 20 TeV for the combined high-energy data sets and as low as 100 GeV for the PS data set. The non-observation of UHECR-neutrino correlations thus extends to even lower energies than considered by Palladino et al. (2020). Even if there were local sources of both UHECRs and neutrinos, they could be transient phenomena, such that the UHECRs emitted over a short period of time arrive much later owing to their deflection, whereas the neutrinos travel on a straight path. It has been estimated by Davoudifar (2011) that the deflection in the EGMF causes a typical time delay on the order of 10^5 yr considering a source distance of 50 Mpc and an EGMF strength of 2 nG. A delay of a couple of decades as expected from propagation in the GMF is already sufficient to decorrelate the observed UHECRs and neutrinos, as the live time of the neutrino and UHECR data sets ranges between 7 and 13 yr.

Another source of uncertainty is the mass composition and thus the charge of UHECRs at the highest energies. The measurements of the UHECR composition above ~ 50 EeV are not yet conclusive. However, several composition constraints at the highest energies (Aab et al. 2014a, 2014b) and the lack of significant, magnetically induced structures in the UHECR arrival directions (Aab et al. 2020a) suggest that less than 10% of UHECRs above ~ 50 EeV might be light elements. Only the light UHECRs are expected to have their source in the vicinity

of their arrival direction as derived from the benchmark deflection model. The sources of heavier UHECRs, e.g., iron nuclei, are spatially almost uncorrelated to the UHECR arrival directions owing to the 26 times larger magnetic deflection compared to protons. We see in analysis 1 that the limits on the neutrino flux are significantly relaxed when assuming a correlation fraction of 50% or 10%. This correlation fraction, defined as the number of UHECRs with a neutrino source in their vicinity, is a simplified model of the UHECR composition.

The modeling of the magnetic deflection as a 2D Gaussian as assumed for analyses 1 and 2 is a simplification with respect to the PT11 and JF12 GMF models (Pshirkov et al. 2011; Jansson & Farrar 2012), which themselves are subject to large uncertainties. Especially in the region of the Galactic plane, we expect deflections that are larger than the assumed mean value of around 3° . In addition, coherent deflection of UHECRs in the GMF and the deflection of UHECRs in the IGMF are not explicitly accounted for. Overall, a coherent shift of UHECRs depending on their arrival direction or an overall significantly larger deflection in the GMF and IGMF can dilute the spatial correlation of UHECRs and neutrinos. Nevertheless, a scaling of the overall deflection is covered partially with the scaling factor applied in analyses 1 and 2, since the overall strength of the deflection and the UHECR charge are largely degenerate parameters.

From a theoretical perspective, the connection of UHECRs and high-energy neutrinos is plausible based on their similar energy budget (Waxman & Bahcall 1999; Bahcall & Waxman 2001; Murase et al. 2013; Ahlers & Halzen 2018). However, this connection could not be proven with the current data and analysis approaches. It is to note that neutrinos with energies in the TeV–PeV range originate most likely from cosmic rays with energies below ~ 100 PeV (Murase & Waxman 2016), which is below the energy threshold of > 50 EeV of the UHECR data sets used here. A direct connection to UHECRs can only be proven with ultra-high-energy neutrinos in the EeV range that have not been discovered yet. The non-observation of a UHECR-neutrino correlation rather points to the possibility that efficient UHECR sources are less efficient neutrino sources and vice versa: sources with efficient UHECR acceleration and emission require an optically thin proton and radiation environment, while sources with dense proton and radiation targets are efficient in neutrino production but not in UHECR emission (Murase et al. 2014; Rodrigues et al. 2021). This argument, however, can be relaxed when considering models, where cosmic rays below ~ 100 PeV are confined in a calorimetric environment and subsequently produce TeV–PeV neutrinos, while a fraction of the cosmic rays are accelerated to the highest energies and escape the source before interacting (Murase & Waxman 2016; Ahlers & Halzen 2018). Although no indication of such a scenario has been found in this analysis, the first indication of such a connection could be the observation of the Seyfert Galaxy NGC 1068 as a potential neutrino source candidate (Aartsen et al. 2020c; Inoue et al. 2020) and UHECR source candidate (Aab et al. 2018). As such sources are numerous also within the UHECR horizon, dedicated future searches correlating UHECR, photon, and neutrino observations might be able to set constraints on specific source candidates, instead of relying on UHECR and neutrino data alone. NGC 1068 could serve as blueprint for a

catalog of potential common sources to be constrained with dedicated analyses.

In summary, the three analyses presented here reflect complementary approaches for tackling the question of a common origin of UHECRs and high-energy neutrinos. Despite substantially enlarged data sets and improved methods, the initially reported results in The IceCube Collaboration et al. (2016) could not be strengthened. For future analyses, we expect substantial gains in sensitivity if the charge of the UHECRs could be estimated on an event-by-event basis, as is expected for future measurements by Auger Prime (Aab et al. 2016).

The authors of the ANTARES collaboration acknowledge the financial support of the funding agencies: Centre National de la Recherche Scientifique (CNRS), Commissariat à l'énergie atomique et aux énergies alternatives (CEA), Commission Européenne (FEDER fund and Marie Curie Program), Institut Universitaire de France (IUF), LabEx UnivEarthS (ANR-10-LABX-0023 and ANR-18-IDEX-0001), Région Île-de-France (DIM-ACAV), Région Alsace (contrat CPER), Région Provence-Alpes-Côte d'Azur, Département du Var and Ville de La Seyne-sur-Mer, France; Bundesministerium für Bildung und Forschung (BMBF), Germany; Istituto Nazionale di Fisica Nucleare (INFN), Italy; Nederlandse organisatie voor Wetenschappelijk Onderzoek (NWO), the Netherlands; Council of the President of the Russian Federation for young scientists and leading scientific schools supporting grants, Russia; Executive Unit for Financing Higher Education, Research, Development and Innovation (UEFISCDI), Romania; Ministerio de Ciencia, Innovación, Investigación y Universidades (MCIU): Programa Estatal de Generación de Conocimiento (refs. PGC2018-096663-B-C41, -A-C42, -B-C43, -B-C44) (MCIU/FEDER), Generalitat Valenciana: Prometeo (PROMETEO/2020/019), Grisolía (refs. GRISOLIA/2018/119, /2021/192) and GenT (refs. CIDEGENT/2018/034, /2019/043, /2020/049, /2021/023) programs, Junta de Andalucía (ref. A-FQM-053-UGR18), La Caixa Foundation (ref. LCF/BQ/IN17/11620019), EU: MSC program (ref. 101025085), Spain; Ministry of Higher Education, Scientific Research and Innovation, Morocco, and the Arab Fund for Economic and Social Development, Kuwait. We also acknowledge the technical support of Ifremer, AIM and Foselev Marine for the sea operation and the CC-IN2P3 for the computing facilities. The ANTARES collaboration acknowledges the significant contributions to this manuscript from Julien Aublin.

The IceCube collaboration acknowledges the significant contributions to this manuscript from Cyril Alispach, Anastasia Barbano, and Lisa Schumacher. The authors of the IceCube Collaboration acknowledge the support from the following agencies: USA—U.S. National Science Foundation-Office of Polar Programs, U.S. National Science Foundation-Physics Division, U.S. National Science Foundation-EPSCoR, Wisconsin Alumni Research Foundation, Center for High Throughput Computing (CHTC) at the University of Wisconsin-Madison, Open Science Grid (OSG), Extreme Science and Engineering Discovery Environment (XSEDE), Frontera computing project at the Texas Advanced Computing Center, U.S. Department of Energy—National Energy Research Scientific Computing Center, Particle astrophysics research computing center at the University of Maryland, Institute for Cyber-Enabled Research at Michigan

State University, and Astroparticle physics computational facility at Marquette University; Belgium—Fonds for Scientific Research (FRS-FNRS and FWO), FWO Odysseus and Big Science programmes, and Belgian Federal Science Policy Office (Belspo); Germany—Bundesministerium für Bildung und Forschung (BMBF), Deutsche Forschungsgemeinschaft (DFG), Helmholtz Alliance for Astroparticle Physics (HAP), Initiative and Networking Fund of the Helmholtz Association, Deutsches Elektronen Synchrotron (DESY), and High Performance Computing cluster of the RWTH Aachen; Sweden—Swedish Research Council, Swedish Polar Research Secretariat, Swedish National Infrastructure for Computing (SNIC), and Knut and Alice Wallenberg Foundation; Australia—Australian Research Council; Canada—Natural Sciences and Engineering Research Council of Canada, Calcul Québec, Compute Ontario, Canada Foundation for Innovation, WestGrid, and Compute Canada; Denmark—Villum Fonden and Carlsberg Foundation; New Zealand—Marsden Fund; Japan—Japan Society for Promotion of Science (JSPS) and Institute for Global Prominent Research (IGPR) of Chiba University; Korea—National Research Foundation of Korea (NRF); Switzerland—Swiss National Science Foundation (SNSF); United Kingdom—Department of Physics, University of Oxford. L.S. and C.H.W. acknowledge financial support from the “Deutsche Forschungsgemeinschaft”.

The successful installation, commissioning, and operation of the Pierre Auger Observatory would not have been possible without the strong commitment and effort from the technical and administrative staff in Malargüe. We are very grateful to the following agencies and organizations for financial support:

Argentina—Comisión Nacional de Energía Atómica; Agencia Nacional de Promoción Científica y Tecnológica (ANPCyT); Consejo Nacional de Investigaciones Científicas y Técnicas (CONICET); Gobierno de la Provincia de Mendoza; Municipalidad de Malargüe; NDM Holdings and Valle Las Leñas; in gratitude for their continuing cooperation over land access; Australia—the Australian Research Council; Belgium—Fonds de la Recherche Scientifique (FNRS); Research Foundation Flanders (FWO); Brazil—Conselho Nacional de Desenvolvimento Científico e Tecnológico (CNPq); Financiadora de Estudos e Projetos (FINEP); Fundação de Amparo à Pesquisa do Estado de Rio de Janeiro (FAPERJ); São Paulo Research Foundation (FAPESP) Grants No. 2019/10151-2, No. 2010/07359-6 and No. 1999/05404-3; Ministério da Ciência, Tecnologia, Inovações e Comunicações (MCTIC); Czech Republic—Grant No. MSMT CR LTT18004, LM2015038, LM2018102, CZ.02.1.01/0.0/0.0/16_013/0001402, CZ.02.1.01/0.0/0.0/18_046/0016010, and CZ.02.1.01/0.0/0.0/17_049/0008422; France—Centre de Calcul IN2P3/CNRS; Centre National de la Recherche Scientifique (CNRS); Conseil Régional Ile-de-France; Département Physique Nucléaire et Corpusculaire (PNC-IN2P3/CNRS); Département Sciences de l'Univers (SDU-INSU/CNRS); Institut Lagrange de Paris (ILP) Grant No. LABEX ANR-10-LABX-63 within the Investissements d'Avenir Programme Grant No. ANR-11-IDEX-0004-02; Germany—Bundesministerium für Bildung und Forschung (BMBF); Deutsche Forschungsgemeinschaft (DFG); Finanzministerium Baden-Württemberg; Helmholtz Alliance for Astroparticle Physics (HAP); Helmholtz-Gemeinschaft Deutscher Forschungszentren (HGF); Ministerium für Innovation, Wissenschaft und Forschung des Landes Nordrhein-Westfalen; Ministerium für Wissenschaft, Forschung und Kunst des Landes Baden-Württemberg; Italy—Istituto Nazionale di Fisica Nucleare

(INFN); Istituto Nazionale di Astrofisica (INAF); Ministero dell’Istruzione, dell’Università e della Ricerca (MIUR); CETEMPS Center of Excellence; Ministero degli Affari Esteri (MAE); México—Consejo Nacional de Ciencia y Tecnología (CONACYT) No. 167733; Universidad Nacional Autónoma de México (UNAM); PAPIIT DGAPA-UNAM; The Netherlands—Ministry of Education, Culture and Science; Netherlands Organisation for Scientific Research (NWO); Dutch national e-infrastructure with the support of SURF Cooperative; Poland—Ministry of Education and Science, grant No. DIR/WK/2018/11; National Science Centre, Grants No. 2016/22/M/ST9/00198, 2016/23/B/ST9/01635, and 2020/39/B/ST9/01398; Portugal—Portuguese national funds and FEDER funds within Programa Operacional Factores de Competitividade through Fundação para a Ciência e a Tecnologia (COMPETE); Romania—Ministry of Research, Innovation and Digitization, CNCS/CCCDI—UEFISCDI, projects PN19150201/16N/2019, PN1906010, TE128 and PED289, within PNCDI III; Slovenia—Slovenian Research Agency, grants P1-0031, P1-0385, I0-0033, N1-0111; Spain—Ministerio de Economía, Industria y Competitividad (FPA2017-85114-P and PID2019-104676GB-C32), Xunta de Galicia (ED431C 2017/07), Junta de Andalucía (SOMM17/6104/UGR, P18-FR-4314) Feder Funds, RENATA Red Nacional Temática de Astropartículas (FPA2015-68783-REDT) and María de Maeztu Unit of Excellence (MDM-2016-0692); USA—Department of Energy, Contracts No. DE-AC02-07CH11359, No. DE-FR02-04ER41300, No. DE-FG02-99ER41107, and No. DE-SC0011689; National Science Foundation, Grant No. 0450696; The Grainger Foundation; Marie Curie-IRSES/EPLANET; European Particle Physics Latin American Network; and UNESCO.

The Telescope Array experiment is supported by the Japan Society for the Promotion of Science (JSPS) through Grants-in-Aid for Priority Area 431, for Specially Promoted Research JP21000002, for Scientific Research (S) JP19104006, for Specially Promoted Research JP15H05693, for Scientific Research (S) JP15H05741, for Science Research (A) JP18H03705, for Young Scientists (A) JPH26707011, and for Fostering Joint International Research (B) JP19KK0074, by the joint research program of the Institute for Cosmic Ray Research (ICRR), The University of Tokyo; by the Pioneering Program of RIKEN for the Evolution of Matter in the Universe (r-EMU); by the U.S. National Science Foundation awards PHY-1404495, PHY-1404502, PHY-1607727, PHY-1712517, PHY-1806797, PHY-2012934, and PHY-2112904; by the National Research Foundation of Korea (2017K1A4A3015188, 2020R1A2C1008230, and 2020R1A2C2102800); by the Ministry of Science and Higher Education of the Russian Federation under the contract 075-15-2020-778, IISN project No. 4.4501.18; and by Belgian Science Policy under IUAP VII/37 (ULB). This work was partially supported by the grants of the joint research program of the Institute for Space-Earth Environmental Research, Nagoya University, and Inter-University Research Program of the Institute for Cosmic Ray Research of University of Tokyo. The foundations of Dr. Ezekiel R. and Edna Wattis Dumke, Willard L. Eccles, and George S. and Dolores Doré Eccles all helped with generous donations. The state of Utah supported the project through its Economic Development Board, and the University of Utah through the Office of the Vice President for Research. The experimental site became available through the cooperation of the Utah School and Institutional Trust Lands Administration (SITLA), U.S. Bureau of Land Management (BLM), and the

U.S. Air Force. We appreciate the assistance of the state of Utah and Fillmore offices of the BLM in crafting the Plan of Development for the site. Patrick A. Shea assisted the collaboration with valuable advice and supported the collaborations’ efforts. The people and the officials of Millard County, Utah, have been a source of steadfast and warm support for our work, which we greatly appreciate. We are indebted to the Millard County Road Department for their efforts to maintain and clear the roads that get us to our sites. We gratefully acknowledge the contribution from the technical staffs of our home institutions. An allocation of computer time from the Center for High Performance Computing at the University of Utah is gratefully acknowledged.

Facility: ANTARES, IceCube Neutrino Observatory, Pierre Auger Observatory, Telescope Array.

ORCID iDs

F. Halzen <https://orcid.org/0000-0001-6224-2417>

References

Aab, A., Abreu, P., Aglietta, M., et al. 2014a, *PhRvD*, **90**, 122005
 Aab, A., Abreu, P., Aglietta, M., et al. 2014b, *PhRvD*, **90**, 122006
 Aab, A., Abreu, P., Aglietta, M., et al. 2015, *ApJ*, **804**, 15
 Aab, A., Abreu, P., Aglietta, M., et al. 2016, arXiv:1604.03637
 Aab, A., Abreu, P., Aglietta, M., et al. 2017, *Sci*, **357**, 1266
 Aab, A., Abreu, P., Aglietta, M., et al. 2018, *ApJL*, **853**, L29
 Aab, A., Abreu, P., Aglietta, M., et al. 2020a, *JCAP*, **2020**, 017
 Aab, A., Abreu, P., Aglietta, M., et al. 2020b, *JInst*, **15**, P10021
 Aartsen, M. G., Abbasi, R., Ackermann, M., et al. 2014a, *JInst*, **9**, P03009
 Aartsen, M. G., Abraham, K., Ackermann, M., et al. 2016, *ApJ*, **833**, 3
 Aartsen, M. G., Abraham, K., Ackermann, M., et al. 2017a, *ApJ*, **835**, 45
 Aartsen, M. G., Abraham, K., Ackermann, M., et al. 2017b, *ApJ*, **835**, 151
 Aartsen, M. G., Ackermann, M., Adams, J., et al. 2014b, *ApJ*, **796**, 109
 Aartsen, M. G., Ackermann, M., Adams, J., et al. 2014c, *PhRvL*, **113**, 101101
 Aartsen, M. G., Ackermann, M., Adams, J., et al. 2017c, *APh*, **92**, 30
 Aartsen, M. G., Ackermann, M., Adams, J., et al. 2017d, *JInst*, **12**, P03012
 Aartsen, M. G., Ackermann, M., Adams, J., et al. 2018a, *PhRvD*, **98**, 062003
 Aartsen, M. G., Ackermann, M., Adams, J., et al. 2018b, *Sci*, **361**, eaat1378
 Aartsen, M. G., Ackermann, M., Adams, J., et al. 2018c, *Sci*, **361**, 147
 Aartsen, M. G., Ackermann, M., Adams, J., et al. 2019, *EPJC*, **79**, 234
 Aartsen, M. G., Ackermann, M., Adams, J., et al. 2020a, *ApJ*, **892**, 53
 Aartsen, M. G., Ackermann, M., Adams, J., et al. 2020b, *ApJL*, **898**, L10
 Aartsen, M. G., Ackermann, M., Adams, J., et al. 2020c, *PhRvL*, **124**, 051103
 Aartsen, M. G., Ackermann, M., Adams, J., et al. 2020d, *PhRvL*, **125**, 121104
 Abbasi, R., Abdou, Y., Ackermann, M., et al. 2013, *NIMPA*, **700**, 188
 Abbasi, R., Ackermann, M., Adams, J., et al. 2021, *PhRvD*, **104**, 022002
 Abbasi, R. U., Abe, M., Abu-Zayyad, T., et al. 2014, *ApJL*, **790**, L21
 Abbasi, R. U., Abe, M., Abu-Zayyad, T., et al. 2018, *ApJL*, **867**, L27
 Abreu, P., Aglietta, M., Ahn, E. J., et al. 2011, arXiv:1107.4809
 Abu-Zayyad, T., Aida, R., Allen, M., et al. 2012, *NIMPA*, **689**, 87
 Ageron, M., Aguilar, J. A., Al Samarai, I., et al. 2011, *NIMPA*, **656**, 11
 Aguilar, J. A., Albert, A., Ameli, F., et al. 2007, *NIMPA*, **570**, 107
 Ahlers, M., & Halzen, F. 2018, *PrPNP*, **102**, 73
 Albert, A., André, M., Anghinolfi, M., et al. 2017, *PhRvD*, **96**, 082001
 Albert, A., André, M., Anghinolfi, M., et al. 2018, *ApJL*, **863**, L30
 Albert, A., André, M., Anghinolfi, M., et al. 2020, *ApJ*, **892**, 92
 Alves Batista, R., Biteau, J., Bustamante, M., et al. 2019, *FrASS*, **6**, 23
 Anchordoqui, L. A., Hooper, D., Sarkar, S., & Taylor, A. M. 2008, *APh*, **29**, 1
 ANTARES Collaboration, Amram, P., Anghinolfi, M., et al. 2002, *NIMPA*, **484**, 369
 Aublin, J., Coleiro, A., Kouchner, A., et al. 2019, *EPJ Web Conf.*, **210** (Les Ulis) in EDP Sciences, [03003](#)
 Bahcall, J., & Waxman, E. 2001, *PhRvD*, **64**, 023002
 Barbano, A. M. 2019, Proc. 36th Int. Cosmic Ray Conf.—PoS (ICRC2019), **358** (Trieste) in SISSA, 842
 Biteau, J., Abreu, P., Aglietta, M., et al. 2022, Proc. 37th Int. Cosmic Ray Conf.—PoS (ICRC2021), **395** (Trieste: SISSA), [307](#)
 Biteau, J., Bister, T., Caccianiga, L., et al. 2019, *EPJ Web Conf.*, **210** (Les Ulis: EDP Sciences), [01005](#)
 Bonifazi, C. & The Pierre Auger Collaboration 2009, *NuPhS*, **190**, 20

Davoudifar, P. 2011, 32nd Int. Cosmic Ray Conf., 2 (Trieste: SISSA), [230](#)

Dawson, B. 2019, Proc. 36th Int. Cosmic Ray Conf.—PoS (ICRC2019), 358 (Trieste) in SISSA, 231

Durrer, R., & Neronov, A. 2013, [A&ARv](#), [21](#), [62](#)

Górski, K. M., Hivon, E., Banday, A. J., et al. 2005, [ApJ](#), [622](#), [759](#)

Haack, C., & Wiebusch, C. 2017, Proc. 35th Int. Cosmic Ray Conf.—PoS (ICRC2017), 301 (Trieste: SISSA), [1005](#)

Iluminati, G., Aublin, J., & Navas, S. 2019, Proc. 36th Int. Cosmic Ray Conf.—PoS (ICRC2019), 358 (Trieste) in SISSA, 920

Inoue, Y., Khangulyan, D., & Doi, A. 2020, [ApJ](#), [891](#), [L33](#)

Jansson, R., & Farrar, G. R. 2012, [ApJ](#), [757](#), [14](#)

Kawai, H., et al. 2008, [NuPhS](#), [175](#), [221](#)

Kopper, C. 2017, Proc. 35th Int. Cosmic Ray Conf.—PoS (ICRC2017), 301 (Trieste) in SISSA, 981

Kronberg, P. P. 1994, [RPPh](#), [57](#), [325](#)

Mészáros, P. 2018, [PhT](#), [71](#), [36](#)

Murase, K. 2015, AIP Conf. Proc. 1666 (Melville, NY) in AIP, [040006](#)

Murase, K., Ahlers, M., & Lacki, B. C. 2013, [PhRvD](#), [88](#), [121301](#)

Murase, K., Inoue, Y., & Dermer, C. D. 2014, [PhRvD](#), [90](#), [023007](#)

Murase, K., & Waxman, E. 2016, [PhRvD](#), [94](#), [103006](#)

Nagano, M., & Watson, A. A. 2000, [RvMP](#), [72](#), [689](#)

Paiano, S., Falomo, R., Treves, A., & Scarpa, R. 2018, [ApJL](#), [854](#), [L32](#)

Palladino, A., van Vliet, A., Winter, W., & Franckowiak, A. 2020, [MNRAS](#), [494](#), [4255](#)

Particle Data Group, Zyla, P. A., Barnett, R. M., et al. 2020, [PTEP](#), [2020](#), [083C01](#)

Pshirkov, M. S., Tinyakov, P. G., Kronberg, P. P., & Newton-McGee, K. J. 2011, [ApJ](#), [738](#), [192](#)

Pshirkov, M. S., Tinyakov, P. G., & Urban, F. R. 2016, [PhRvL](#), [116](#), [191302](#)

Rodrigues, X., Heinze, J., Palladino, A., van Vliet, A., & Winter, W. 2021, [PhRvL](#), [126](#), [191101](#)

Schumacher, L. 2019, EPJ Web Conf., 207 (Les Ulis: EDP Sciences), [02010](#)

Sommers, P. 2001, [APh](#), [14](#), [271](#)

Stettner, J. 2019, Proc. 36th Int. Cosmic Ray Conf.—PoS (ICRC2019), 358 (Trieste) in SISSA, 1017

The IceCube Collaboration 2013, [Sci](#), [342](#), [1242856](#)

The IceCube Collaboration The Pierre Auger Collaboration & The Telescope Array Collaboration 2016, [JCAP](#), [2016](#), [037](#)

The Pierre Auger Collaboration 2015, [NIMPA](#), [798](#), [172](#)

Tkachev, I., Fujii, T., Ivanov, D., et al. 2021, Proc. 37th Int. Cosmic Ray Conf.—PoS (ICRC2021), 395 (Trieste) in SISSA, 392

Tokuno, H., Tameda, Y., Takeda, M., et al. 2012, [NIMPA](#), [676](#), [54](#)

Troitsky, S., Fukushima, M., Ikeda, D., et al. 2017, Proc. 35th Int. Cosmic Ray Conf.—PoS (ICRC2017), 301 (Trieste) in SISSA, 548

Wandkowsky, N. 2018, [XXVIII Int. Conf. on Neutrino Physics and Astrophysics](#), [501](#)

Waxman, E., & Bahcall, J. N. 1999, [PhRvD](#), [59](#), [023002](#)